DOKUZ EYLÜL UNIVERSITY
GRADUATE SCHOOL OF NATURAL AND APPLIED SCIENCES

APPLICATION OF DEEP LEARNING TO CLASSIFICATION OF ACOUSTIC EMISSION (AE) MEASUREMENTS FOR DAMAGE DETECTION IN COMPOSITES

by
Şevki Onur DORUK

April, 2021
İZMİR

APPLICATION OF DEEP LEARNING TO CLASSIFICATION OF ACOUSTIC EMISSION (AE) MEASUREMENTS FOR DAMAGE DETECTION IN COMPOSITES

A Thesis Submitted to the
Graduate School of Natural And Applied Sciences of Dokuz Eylül University
In Partial Fulfillment of the Requirements for the Degree of Master of Science in Mechanical Engineering

by

Şevki Onur DORUK

April, 2021
İZMİR

M.Sc THESIS EXAMINATION RESULT FORM

We have read the thesis entitled "**APPLICATION OF DEEP LEARNING TO CLASSIFICATION OF ACOUSTIC EMISSION (AE) MEASUREMENTS FOR DAMAGE DETECTION IN COMPOSITES**" completed by **ŞEVKİ ONUR DORUK** under supervision of **PROF. DR. AYŞE SAİDE SARIGÜL** and we certify that in our opinion it is fully adequate, in scope and in quality, as a thesis for the degree of Master of Science.

....

Prof. Dr. Ayşe Saide SARIGÜL

Supervisor

....

Prof. Dr. Yeliz PEKBEY

Jury Member

....

Prof. Dr. Abdullah SEÇGİN

Jury Member

Prof.Dr. Özgür ÖZÇELİK
Director
Graduate School of Natural and Applied Sciences

ACKNOWLEDGEMENTS

First and foremost I would like to thank Professor Ayşe Saide SARIGÜL for her guidance and continuous support during my Master studies.

I must also thank Professor Dirk SÖFFKER who gave me a chance to study in his research group as an exchange student and complete this thesis. I am also grateful to Dr. Sebastian Felix WIRTZ for his advice and assistance during this project.

Finally, I would like to thank all of my family for supporting me throughout the years.

Şevki Onur DORUK

APPLICATION OF DEEP LEARNING TO CLASSIFICATION OF ACOUSTIC EMISSION (AE) MEASUREMENTS FOR DAMAGE DETECTION IN COMPOSITES

ABSTRACT

Composites offer high strength and stiffness with lightweight, making them attractive for a wide range of engineering applications. However, complex fracture mechanics of composites leading high maintenance costs and safety concerns especially in safety-critical applications. In particular, some of damage modes such as matrix cracking, delamination and fiber breakage may cause critical failures in specific applications. Therefore, development of effective and reliable Structural Health Monitoring (SHM) systems which are capable of detecting and identifying damage is necessary. Acoustic Emission (AE) is particularly suitable to be used in SHM systems due to its passive nature which enables in-situ and in real-time monitoring. Additionally, deep learning-based methods such as Convolutional Neural Networks (CNN) improved the state-of-the-art in image classification tasks and are used in different domains successfully. In contrast, a little attention has been paid to apply this method on characterization of damage in composites. In this study, CNN based classification scheme is used to classify AE measurements and dependence of classification performance on different propagation distances is investigated experimentally. Different damage modes are represented by the dominant fundamental Lamb wave modes which are generated using artificial AE source. The generated labelled waveforms are measured by sensors mounted at different distances to AE source. Two different architectures of CNN model are used to classify AE measurements and the performance of CNN models is evaluated. Finally, investigation of transfer learning concept for the sensors mounted at different positions is conducted.

Keywords: Acoustic emission, composite, convolutional neural networks, deep learning, diagnosis

KOMPOZİTLERDEKİ HASAR TEŞHİSİ İÇİN AKUSTİK EMİSYON (AE) SINIFLANDIRMASINDA DERİN ÖĞRENMENİN UYGULANMASI

ÖZ

Kompozitler sahip oldukları yüksek mukavemet ve rijitlikten ötürü birçok mühendislik uygulamasında tercih edilmektedir. Fakat aynı malzemelerde görülen kompleks hasar mekaniği, güvenlik tehlikesi taşıyan uygulamalarda yüksek bakım masrafları ve fonksiyonel güvenlik endişelerinide beraberinde getirmektedir. Özellikle matris kırığı, delaminasyon ve fiber kopması gibi farklı hasar mekanizmalarından bazıları uygulama tipine göre ciddi olumsuz sonuçlar doğurabildiğinden, bu hasar modlarını anlık olarak tespit edebilen etkili ve güvenilir yapısal durum izleme sistemlerine ihtiyaç duyulmaktadır. Akustik emisyon yöntemi, yerinde ve gerçek zamanlı tespite imkan veren yapısı gereği yapısal durum izleme sistemlerinde kullanılmaya elverişlidir. Bunun yanında, resim tanıma-sınıflandırma görevlerinde çitayı oldukça yükseltmiş olan konvolüsyonel sinir ağları (CNN) gibi derin-öğrenme yöntemleri farklı disiplinlerde başarıyla kullanılmaktadır. Buna karşın, bu metodun kompozitlerdeki hasar modlarının tespitinde kullanılmasına dönük fazlaca bir çalışma bulunmamaktadır. Bu çalışmada akustik emisyon ölçümleri konvolüsyonel sinir ağları ile sınıflandırmaya tabi tutulmuş ve sınıflandırma performansının farklı yayılım uzaklıklarından nasıl etkileneceği deneysel olarak kompozit plaka üzerinde incelenmiştir. Farklı hasar tiplerini temsilen yapay akustik emisyon kaynakları olarak temel Lamb dalga modları kullanılmıştır. Üretilen ve sınıfları belirli olan dalgalar kaynaktan farklı uzaklıklıklarda ölçülerek iki farklı mimariye sahip konvolüsyonel sinir ağı modeli tarafından sınıflandırmaya tabi tutulmuştur. Modellerin sınıflandırma performansı dalga yayılım etkileri gözönünde bulundurularak değerlendirilmiştir. Son olarak farklı pozisyonlarda bulunan sensörler için öğrenme transferi konseptinin uygulanması araştırılmıştır.

Anahtar kelimeler: Akustik emisyon, kompozit, konvolüsyonel sinir ağları, derin öğrenme, hasar tespiti

CONTENTS

Page

LIST OF FIGURES

Page

LIST OF TABLES

Page

CHAPTER ONE
INTRODUCTION

Composite materials offer high strenght and high stiffness with lightweight, which makes them attractive for a wide range of engineering applications, especially for the aviation industry. Airframe of new generation airplanes comprises 50% advanced composites, such as Boeing 787 and Airbus A350, enabling 20% of weight reduction compared to more conventional aluminum designs (Boeing, 2006). According to Giurgiutiu (2015), adoption of high performance composites into civil aviation is still upward trend due to strict emission regulations. In addition to aviation industry, growth of composite usage is also ongoing trend in other transport applications, wind turbines, large-scale structures such as pipelines and pressure vessels.

Despite many attractive properties, complex fracture mechanics of the composites is leading high maintenance costs and safety concerns. The brittle nature of the material prevents the detecting damage by utilizing the visual inspection methods, although the structure suffers from the damage internally. Furthermore, different micro-mechanical damage modes such as matrix cracking, delamination or fiber breakage make the assessment of the damage more complicated. Therefore, development of effective and reliable Structural Health Monitoring (SHM) systems is necessary for using on composite materials and structures.

SHM relies on observation of a structure or mechanical system by sensor measurements and evaluation of those measurements using statistical methods to determine the current state of system health (Farrar & Worden, 2007). In order to assess health of the structure, SHM systems need to fulfill different tasks such as detection, identification and localization of damage (Eaton et al., 2011).

Acoustic Emission (AE) is a highly sensitive non-destructive testing method, which is particularly suitable to be used in SHM systems due to its passive nature which enables in-situ and in real-time monitoring. The method is based on measuring elastic transient waves, which is released by the structure when the material is under stress. The measured waveforms contain damage-specific signatures and analysis of those measurements enables information about the damage. The main challenge of analysis of AE is that the waveform of emitted elastic waves changes due to propagation effects such as attenuation and dispersion while the waves are propagating through the structure before they are measured by sensors. Furthermore, these propagation effects are particularly strong in composite materials.

In order to find damage-specific signatures and identify different damage modes in composites, many different pattern recognition techniques have been used in literature. Deep learning-based methods improved the state-of-the-art in image and speech recognition in addition to many other domains such as medical studies and genomics (LeCun et al., 2015). Convolutional Neural Networks (CNN) is a deep neural network, which does not require manual feature extraction unlike other conventional pattern recognition techniques (Ebrahimkhanlou & Salamone, 2018). Despite the achievement of CNN on various classification tasks in different domains, little attention has been paid to apply this method on characterization of damage in composites. Furthermore, it has not been demonstrated that how classification performance is affected by different propagation distances.

In this study dependence of classification performance on different propagation distances is investigated experimentally. Different damage modes are represented by the dominant fundamental Lamb wave modes which are generated using artificial AE source. The generated labelled waveforms are measured by sensors mounted at different distances to AE source. Two different architectures of CNN model are used to classify AE measurements and the performance of the CNN models is evaluated with particular focus on propagation effects. Finally, investigation of transfer learning concept for the sensors mounted at different positions is conducted.

The study is divided into 6 chapter. The second chapter gives a brief overview of past studies related to AE and damage characterization in composites. Chapter 3, addresses the theoretical concepts related to this study. Chapter 4, introduces the experimental framework and CNN architectures used for classifications tasks. The results are presented in Chapter 5. Finally, Chapter 6 summarized the present study.

CHAPTER TWO
LITERATURE REVIEW

Acoustic Emission (AE) is used to address different problems related to damage in composite materials, such as damage detection and characterization, damage localization as well as damage evaluation and useful life time estimation (Godin et al., 2018). In this section, previous works related to AE based damage characterization in composites are reviewed.

The ortothropic nature of the composites leads different damage modes in the structure. AE technique is used to identify these micro-mechanical damage modes such as matrix cracking, delamination, fiber breakage and fiber pull-out by associating AE sources with those damage modes (Kishi et al., 2000).

The studies which use AE regarding damage characterization problem in composites are based on applying particular loading conditions to a structure to lead individual micro-mechanical damage mode while recording AE activity. According to Gutkin et al. (2011), "AE signal can be characterized using three main techniques: (i) classification using single parameter such as amplitude or frequency, (ii) classification according to several parameters using pattern recognition techniques, (iii) classification according to modal content such as extensional and flexural modes".

The early studies used time-domain descriptors such as amplitude as a descriptor to identify different damage modes and associated particular amplitude ranges with individual failure modes (Barre & Benzeggagh, 1994). However, some of the studies suggested different amplitude ranges for particular damage modes for same type of specimens (Berthelot & Rhazi, 1990; Valentin et al., 1983).

Ni & Iwamoto (2002) investigated the effect of propagation path on AE parameters such as amplitude and frequency. The study showed that amplitude is strongly attenuated during the propagation, while frequencies of the measured waveforms are not affected by increased propagation distance. The authors suggested that frequency analysis of AE signal is more effective instead of using amplitude as a descriptor regarding damage identification problem in composites.

De Groot et al. (1995) used frequency-based analysis on carbon/epoxy material in a form of unidirectional composite. In this study, the specimens that are designed to be failed in particular damage modes are loaded until the failure and the frequency of AE activities are obtained in real-time using spectrum analyzer. The results showed that matrix cracking emits a waveform in a frequency range between 90-180 kHz, fiber breakage released a signal with frequency above 300 kHz. Fiber pull-out emitted a signal in a frequency range between 180-240 kHz and fiber-matrix debonding generated a signal between 240-310 kHz. Ramirez-Jimenez et al. (2004) used frequency-based analysis on glass/polypropylene specimens. The authors obtained peak frequencies of measured waveforms by means of a Fast Fourier Transform (FFT) and observed a relation between micro-mechanical damage modes and specific frequencies. The results showed that peak frequency is recorded at 100 kHz during matrix-fiber debonding failure. Fiber breakage led to waveforms with 420 kHz and 520 kHz peak frequencies in different tests.

The studies which obtained frequency spectrum of AE signal using FFT revealed the frequency content of AE signal without time resolution. In contrast, AE measurements include AE sources leading non-stationary behaviour in emitted signal. Therefore, time-frequency analysis methods enable more useful information about AE source by revealing when the frequency component occurs in measured signal. Baccar & Soeffker (2017) used Continuous Wavelet Transform (CWT) to obtain time-frequency representation of measured AE signal and examined peak frequencies using obtained scalogram.

The recent studies used pattern recognition techniques which use several AE parameters simultaneously (Gutkin et al., 2011; Baccar & Soeffker, 2017). The pattern recognition techniques can be either supervised or unsupervised. In supervised techniques, training data is given to algorithm to associate those signals with labels, so associates with different damage modes in characterization problem (Godin et al., 2004). In contrast, unsupervised techniques group signals which show similar characteristics without the training data is given to algorithm (Crivelli et al., 2014).

The conventional pattern recognition techniques require manual feature extraction, which may lead to the loss of useful information in a raw data. Therefore, design of feature extractors requires special attention and quite developed domain expertise (LeCun et al., 2015). In contrast, deep learning approaches eliminate manual feature extraction and obtain the representations automatically during the learning process. Abdeljaber et al. (2017) used 1D convolutional neural networks in vibration-based damage detection. Ebrahimkhanlou & Salamone (2018) used two different deep learning methods, the stacked autoencoders and convolutional neural networks, to solve localization problem in a plate-like structure made of composite. The authors used pencil lead break tests as artificial AE sources to simulate fatigue cracks. CWT is used to obtain time-frequency representation of waveforms. Furthermore, CWT coefficients of the measured waveforms are converted into RGB images and used input for CNN models. The authors reported that both of the deep learning architectures, the stacked autoencoders and convolutional neural networks, successfully localized AE sources on test data. Tabian et al. (2019) used CNNs to detect, identify and localize the impact damage in composites. Reportedly, the proposed CNN models detected and identified the energy levels of each impact source with high accuracy in addition to localizing AE sources.

Maillet et al. (2015) investigated the effects of attenuation on AE signal features and reported change in frequency centroid of AE signal during the propagation. Attenuation effects on AE signal is also examined by Wirtz et al. (2019) experimentally. The authors reported the dependence of attenuation on frequency of AE waveform in addition to applied load conditions on structure. Asamene et al. (2015) suggested that attenuation is also dependant of modal content of AE signal. The authors reported that fundamental asymmetrical mode A0 is more strongly attenuated compared to fundamental symmetrical mode S0 in carbon/epoxy laminate.

CHAPTER THREE
THEORETICAL BACKGROUND

3.1 Composites

3.1.1 Overview

The following information about composites is based on the work of Mazumdar (2001).

Composite is defined as a "material which is made by combining two or more materials to enable specific properties by combining the characteristics of individual materials". The generic definition in above includes also metallic alloys, plastic co-polymers, minerals and woods. However, fiber reinforced composites are different from those materials in a way: constituent materials of the fiber reinforced composites, reinforcement and matrix material, work together in bulk structure but they preserve their individual form and can be separated from each other by mechanical methods.

The typical composites are formed by reinforcement element such as fibers. These fibers are bonded by a matrix element such as polymer resin or ceramics and form the structure. The reinforcing fibers provide strength and stiffness to the structure, while the matrix element enables rigidity and environmental resistance. This orthotropic nature enables a wide range of attractive mechanical properties as leading complex fracture mechanics.

Different micro-mechanical damage modes such as matrix cracking, fiber breakage, fibermatrix debonding and delamination can be observed as a result of loads applied on Carbon Fiber Reinforced Polymer (CFRP) structure. Figure 3.1 illustrates different damage modes in CFRP structures.

Composite materials have been used to solve different engineering problems for a long time. However, the industrial interest into this material has started with

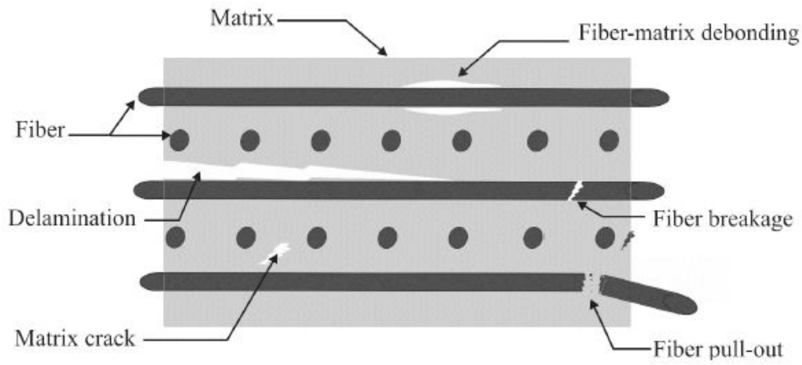

Figure 3.1 Damage modes in CFRP (Baccar, 2015)

establishment of polymeric-based composites in 1960. Today, composites are common engineering material in different engineering applications such as automotive components and aerospace parts, consumer goods, in marine and oil industries. The increase in usage of composites instead of conventional materials such as steel and aluminium is a result of superior properties of composites which enables better product performance and especially their lightweight characteristic. Composites have high specific strength and specific stiffness compared to steel and aluminium, making them attractive as an engineering material. Furthermore, fatigue strength of composites are higher than the traditional metals. In addition to mechanical properties, the composites offer high corrosion and chemical resistance because their outer surface is formed by polymer based materials. There are also some design and manufacturing flexibilities such as several metallic parts in a design can be replaced by a single composite part. Moreover, complex parts which require additional manufacturing processes such as machining or welding when the metallic material is used, can be manufactured in a single process as composite structure.

3.2 Acoustic Emission

3.2.1 Overview

Acoustic Emission (AE) is a term that defines both a phenomenon and Non-Destructive Testing (NDT) method which is developed from this phenomenon.

The American Society for Testing of Materials (ASTM) defines acoustic emission as "the set of phenomenon in which transient elastic waves are generated by dissipation of energy from sources located within a material" (ASTM, 2017).

Loads which are applied to structure create micro-displacements, which lead to generation of elastic waves. Nature and frequency of generated waves depend on their sources. Release of rapidly localized energy gives rise to elastic waves which are in ultrasonic range and those waves propagate through the structure after they are released. Surface displacements due to those waves can be detected by using highly sensitive sensors and the obtained waveforms can be analyzed to distinguish different source mechanisms, though those waveforms go some modifications during the propagation due to propagation effects such as attenuation and dispersion. AE includes examination and characterization of these waveforms with their relevant damage mechanisms. In addition to detecting and identifying damage mechanisms, localization problem also can be addressed by AE.

AE, listening the structure without any external excitation, is a passive NDT method enabling monitoring damage in situ and in real time. Therefore, AE is one of the most frequently used NDT methods within the studies which address the Structural Health Monitoring (SHM) systems. Furthermore, AE is also remarkable for identifying different micro-mechanical damage mechanisms in different type of composites such as organic matrix, metallic or ceramic matrix composites (Godin et al., 2018). The most commonly used NDT methods and their abilities to identify different damage mechanisms in composite materials are shown in Table 3.1

In principle, AE signals can be grouped as burst and continuous-acoustic emission signal. Burst or discrete emission signal, which is in the form of damped sine wave, indicates individual AE event. However, continuous emission is in the form of noise due to rapidly occurred and overlapped AE events as it is illustrated in Figure 3.2. The burst signal is associated with crack initiation and propagation, whereas continuous emission signal is related to dislocation movement which is observed while the plastic deformation occurs in metals (Godin et al., 2018).

Table 3.1 Main techniques used for identification of damage in composites (Godin et al., 2018)

	Acoustic emission	C-scan ultrasound	X-ray	Microscopy	High Res. X-ray
Fiber rupture	Possible	No	Possible	Non-destructive destructive	Possible
Delamination	Possible	Yes	Yes	On the edge or destructive	Possible
Matrix cracking	Possible	No	Yes	On the edge or destructive	Possible
Decohesion	Possible	No	No	Non-destructive destructive	Possible

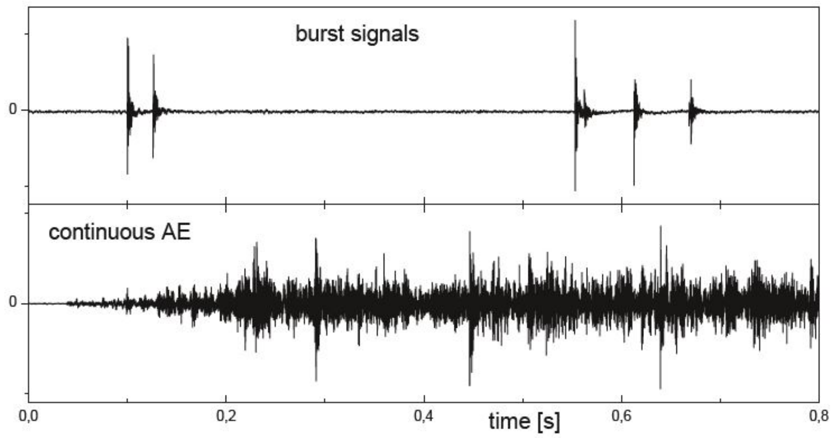

Figure 3.2 Example of burst and continous emission signal (Grosse & Ohtsu, 2008)

In addition to AE source events related to material degradation such as defect growth, crack advance or plastic deformation, there are wide range of acoustic emission source events which enables monitoring different industrial processes such as crystallographic phase transformations, melting and solidification; welding noise, forging, machining, drilling, grinding; flow of single and two phase fluids, leaks and boiling (Scruby, 1987).

Furthermore, there are also artificial AE sources, which enables to simulate AE sources in experimental studies. The most widely used artificial source is Pencil Lead Break (PLB), also known as Hsu-Nielsen source. In this method, mechanical pencil lead is pressed against a surface of a structure firmly until the occurrence of lead breakage. Illustration of method can be seen in Figure 3.3.

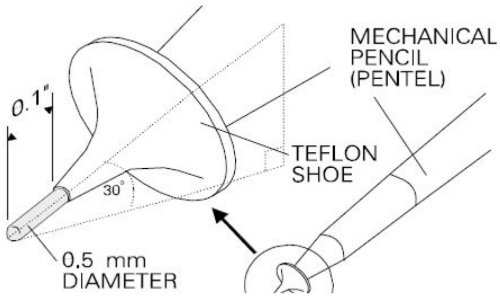

Figure 3.3 Hsu-Nielsen source (Hellier, 2003)

As a result of a sudden released stress, the surface starts to vibrate in micro scale and generates elastic wave which propagates in the structure (Sause, 2011). The resulting waveform is quite similar to waveforms obtained by the sources of real damage (Kharrat et al., 2018). Due to easy handling procedure of Hsu-Nielsen source, this artificial source became the most commonly used test source not only in practical applications, but also in laboratory environment (Sause, 2011). Hsu-Nielsen source is typically used to verify functionality of coupling, sensors and electronic equipment. In practical applications which require wide area monitoring, PLB is a criteria to specify maximum permissible sensor spacing based on ability to detect PLB sources in measurements taken in the whole inspection area (Hellier, 2003). Furthermore, the propagation properties of the structure under inspection can be obtained by using PLB sources.

The PLB sources are monopole sources; however, the most of the stress-induced AE sources are dipole sources. Moreover, real sources are buried in the structure, whereas PLB sources induce the stress waves at surface level. Hamstad (2007) investigated the effects of source characteristics on AE signal by using finite element models and comparing them with experimental results. The study showed that PLB sources which is acted on surface are well representation of buried monopole sources. Moreover, the same study revealed that in-plane PLB sources are better at representing modal intensity (A_0 and S_0) compared to out-of-plane PLB sources. In another study, Sause (2011) showed that slight differences on free lead length or contact angle during the applying PLB source cause large changes in source magnitudes. The present study aims to use an artificial source which is able to provide wide variety of sources, associated with different damage mechanisms, to be classified by neural network models. In addition to request of variety of sources, the reproducibility of the source is an important characteristic for our experiment to provide large number of training data for neural networks model.

If a structure is subjected to stress which causes to plastic deformation on structure, AE events follow irreversible process. This phenomenon is explained by Kaiser effect and is illustrated in Figure 3.4a. While the material undergoes plastic deformation with increasing loading conditions, AE events start to occur in an individual point and increases with applied load. After the structure is unloaded and reloaded respectively, AE events only start when the load exceeds to highest load point (F1) in primary loading case. If AE event starts before the load reaches to F1, it indicates the damage occurrence in a stress history of the structure. This phenomenon is illustrated in Fig3.4. The ratio of the load which AE events starts (F2), to a maximum load point (F1) which is reached at past loading gives the felicity ratio as

$$R_F = \frac{F_2}{F_1}, \tag{3.1}$$

where R_F stands for felicity ratio which is a measure of the structural integrity and used for determining the health of the observed structure. It should be noted that, if the felicity ratio of the loaded structure is equal to 1, this means that the structure is undamaged and follows Kaiser effect.

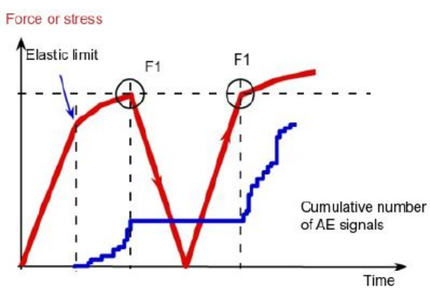

(a) Kaiser effect

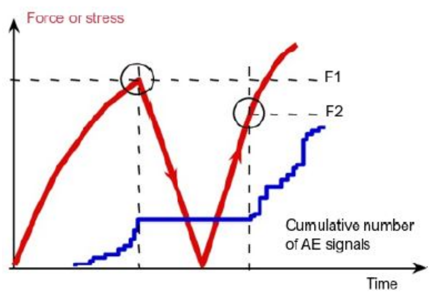

(b) Felicity ratio

Figure 3.4 Kaiser effect and Felicity ratio (Godin et al., 2018)

3.2.2 Ultrasonic Elastic Waves in Solid Media

Ultrasonic elastic waves which are generated as a result of AE phenomenon start to propagate in a structure immediately after they are emitted. In AE method these waves are measured by sensors mounted on surface of the structure and their waveforms are examined to find damage-specific signatures. However, the waveforms undergo propagation effects while they are propagating through the structure before reaching the surface (Godin et al., 2018). Therefore, it is important to consider propagation effects on AE measurements to be able to analyse AE signal correctly. This chapter presents the fundamental concepts of elastic waves and wave propagation, which is related to AE.

3.2.2.1 Longitudinal and Transverse Waves

Elastic waves propagate in infinite media, in which the boundaries have no effect on propagation, in two different forms: transverse waves and longitudinal waves. In transverse waves, the particle motion is perpendicular to propagation direction, whereas in longitudinal waves the particles move parallel to propagation direction (Eaton, 2007). Transverse and longitudinal waves, also known as bulk waves, are illustrated in Figure 3.5.

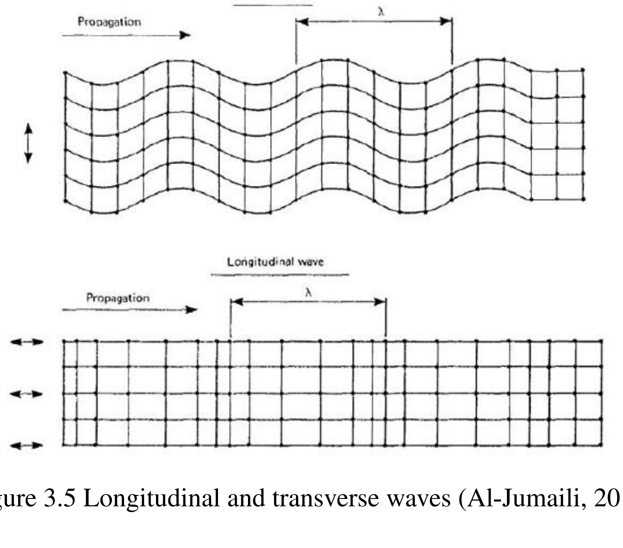

Figure 3.5 Longitudinal and transverse waves (Al-Jumaili, 2016)

3.2.2.2 *Rayleigh Waves*

If a surface is introduced as a boundary, transverse and longitudinal waves form Rayleigh waves in a close region to the surface (Eaton, 2007). The illustration of Rayleigh waves can be seen in Figure 3.6. In Rayleigh waves, particles of solid medium move in an elliptical path, in which major axis of ellipse path is perpendicular to the surface of solid. The width of elliptical path decreases as the depth increases from surface (Russel D., 2016). Rayleigh waves can be observed in a surface of thick structures such as thick plate where the wavelength is relatively small compared to thickness of structure (Rose, 2014).

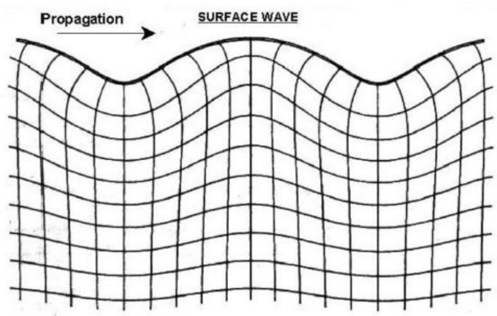

Figure 3.6 Rayleigh waves (Al-Jumaili, 2016)

3.2.2.3 *Lamb Waves*

In a plate-like structure, in which two surfaces are introduced as a boundary, bulk waves interact with each other and the both surfaces. As a result, two fundamental modes of wave propagation, namely symmetrical (extensional) and asymmetrical (flexural) modes are observed. Illustration of symmetric and asymmetric waves, also known as Lamb waves, can be seen in Fig 3.7.

Symmetric and asymmetic lamb modes in isotropic plate can be formulated as

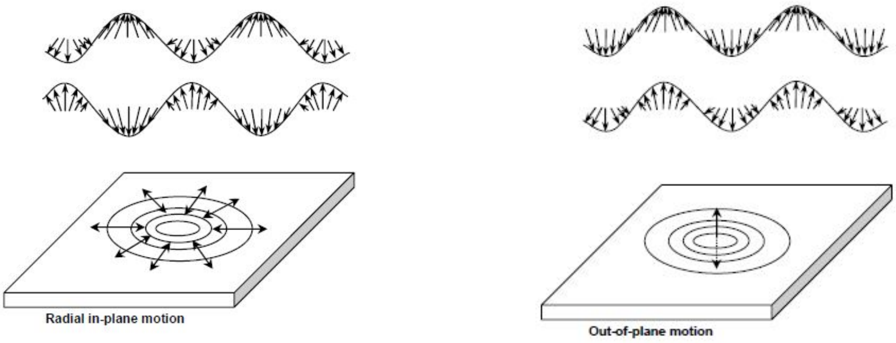

(a) Symmetrical Lamb wave (Extensional)   (b) Asymmetical Lamb wave (Flexural)

Figure 3.7 Lamb waves (Su & Ye, 2009)

follows,

$$\frac{tan(qh)}{tan(ph)} = -\frac{4k^2qp}{(k^2-q^2)^2}, \tag{3.2a}$$

$$\frac{tan(qh)}{tan(ph)} = -\frac{(k^2-q^2)^2}{4k^2qp}, \tag{3.2b}$$

$$p^2 = \frac{\omega^2}{c_L^2} - k^2, \tag{3.2c}$$

$$q^2 = \frac{\omega^2}{c_T^2} - k^2, \tag{3.2d}$$

$$k = \omega / c_p, \tag{3.2e}$$

where $h, k, c_L, c_T, c_p, \omega$ are the plate thickness, wave number, velocities of longitudinal and transverse modes, phase velocity and wave circular velocity, respectively (Su et al., 2006). Eq.3.2a and Eq.3.2b, known as Rayleigh-Lamb equations for symmetrical and asymmetrical Lamb waves respectively, are transcendental equations, which can be solved numerically. Related equations correlating the propagation velocity with its frequency imply that Lamb waves are dispersive (Su et al., 2006).

3.2.2.4 Velocity and Dispersion

Solution of Rayleigh-Lamb equations (Eq.3.2) is used to determine the velocity of a wave of particular frequency or product of frequency and thickness in a wave mode (Rose, 2014). For a given product of plate thickness and frequency, different Lamb modes may exist together (Su et al., 2006). However, amplitude of higher order modes are significantly less than fundamental modes, symmetric mode (S_0) and asymmetric mode (A_0) and hence their usage is limited in AE method (Eaton, 2007).

Figure 3.8 illustrates a dispersion curve, produced by commercial software *Disperse*, which describes the propagation of Lamb wave modes for 2.15 mm thick cross-ply composite laminate. As seen in the figure, S_0 mode has significantly high velocities compared to A_0 mode at low frequencies.

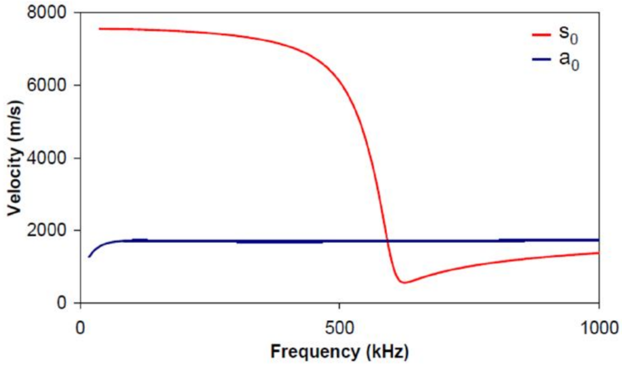

Figure 3.8 Dispersion curve for composite material (Eaton, 2007)

The wave dispersion phenomenon can be illustrated with propagation of single frequency wave packets or bursts as illustrated in Figure 3.9.

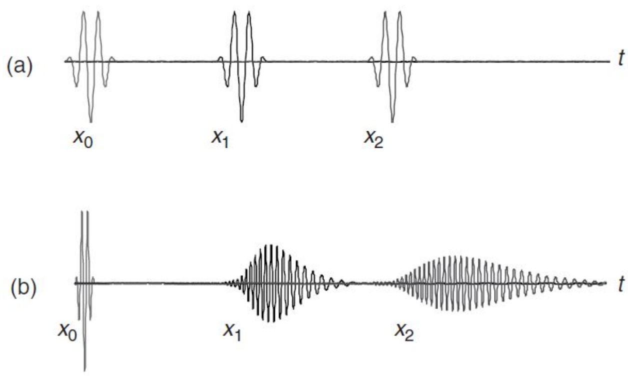

Figure 3.9 Propagation of tone-burst in a) Non-dispersive constant wave-speed b) Dispersive frequency dependant wave speed (Giurgiutiu, 2007)

Burst signal consists of different frequencies as a result of modulation operation on single frequency wave. When every individual frequency in a wave packet propagates in same velocity, burst preserves its shape as seen in Figure 3.9a. In contrast, if the harmonics propagate with different velocities, the shape of the wave packet changes as it propagates, which is illustrated in Figure3.9b. As a result of dispersion, the wave packet has stretched out and elongated.

The intensity of the dispersion in tone-burst is connected with the wave-packet length. Figure 3.10 illustrates how the frequency spectrum changes as the wave packet length varies. In a case of the wave packet has a long length, meaning number of wave cycle (N_c) or counts of wave packet is relatively large number, the frequency spectrum becomes narrow and close to the single carrier wave frequency as shown in Fig. 3.10a. However, if the wave packet length is short, its frequency spectrum covers wide frequency range, meaning the wave has more dispersive characteristic as illustrated in Fig 3.10b.

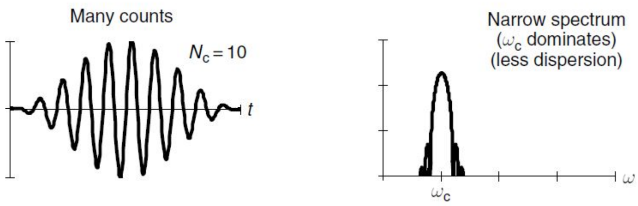

(a) Frequency spectra of N_c = 10 burst signal

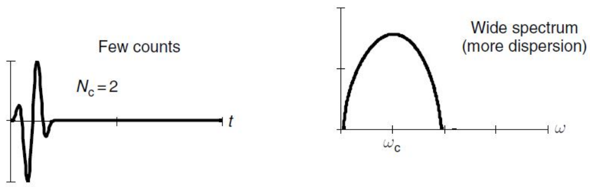

(b) Frequency spectra of N_c = 2 burst signal

Figure 3.10 Effect of length of burst to the frequency spectra (Giurgiutiu, 2007)

If the wave consists of one single frequency, the waveform preserves its shape along the propagation. In that case velocity of the waveform can be defined by phase velocity as

$$C_p = f\lambda, \tag{3.3}$$

$$k = \frac{\omega}{C_p}, \tag{3.4}$$

where C_p, f and λ stand for phase velocity, frequency and wave length respectively. Equation 3.4 relates the wave number (k) with the radial frequency (ω).

However, if the wave-packet consists of different frequencies such as burst, the propagation behaviour of the whole package described by group velocity. Group velocity is the velocity at which transportation of energy of signal occurs (Eaton, 2007) and varies with frequency according to:

$$C_g = \frac{\partial \omega}{\partial k}. \tag{3.5}$$

3.2.2.5 Attenuation

Attenuation is defined as decrease in amplitude of elastic wave with propagation distance (Prosser, 1996). Individual mechanisms which have role in attenuation phenomenon are described by Pollock (1986):

- **Geometric Spreading** Geometric spreading is dominant attenuation effect in a close area to AE source. The spherical radiation of energy from the source causes a reduction in amplitude with propagation distance (Sause, 2011). The quantity of attenuation for plates is inversely proportional to the square root of propagation distance. Therefore, attenuation effect of geometric spreading is equivalent to 40 dB, which is significant value, after a few centimetres propagation. In plates, the attenuation in this area can be greater than this value because of the separation of different modes and velocity dispersion (Prosser, 1996).

- **Internal friction** Internal friction, also known as absorption, describes loss of elastic energy as a result of micro material interactions, causing to produce heat while the wave is propagating. Effect of internal friction is stronger in composite materials, in which viscoelastic material behaviour can be related to those losses (Eaton, 2007). Attenuation which is caused by internal friction is more powerful in the far field of AE source. The amplitude decreases exponentially with propagation distance. Furthermore, this type of attenuation effect is stronger at high frequencies (Eaton, 2007). The attenuation coefficient α can be found experimentally. For plate waves, absorption becomes more dominant compared to geometric spreading in a distance, which is formulated by $4.34/\alpha$ to the source (Prosser, 1996).

- **Velocity dispersion** Dispersion is a change in waveform as a result of different propagation velocities of harmonics, which are involved in a signal. The level of attenuation caused by dispersion depends on the frequency content of signal and the dispersion curve. Prosser (1996) reported that the flexural mode attenuation is significantly larger than extensional mode in measurements carried out in a far field to source. The results were the same even though extensional mode consists of much higher frequencies, which are easily attenuated by absorption mechanisms. Therefore, the effect of dispersion on amplitude attenuation can be considered more dominant compared to other attenuation effects.

- **Dissipation into adjacent media** If the structure which is going to be examined in AE testing is contacted with adjacent media the elastic waves are transmitted into related media. Therefore, energy of signal is reduced (Sause, 2011). For instance, propagation of waves into out of pipe or into fluid which is contained in a pressure vessel which is under examination corresponds the related attenuation. Furthermore, the same attenuation effect can be seen in individual material which has inhomogeneous material properties leading to scattering of waveform at the interfaces such as reinforcement of composites or grain boundaries of metals (Prosser, 1996).

3.2.3 Sensing and Data Acquisition

AE analysis is based on examining the waveforms generated by AE sources. These waveforms are obtained by highly sensitive transducers or sensors, converting surface displacements into electrical signal which is going to be amplified by pre-amplifiers before the signal is digitized (Scruby, 1987). Typical measurement chain of AE consists of piezoelectric sensors, pre-amplifiers and data acquisition system (Godin et al., 2018).

There are different types of transducers in AE such as non-contact optical sensing, fiber optic sensing and capacitive sensing (Ozevin et al., 2006). However, piezoelectric sensors including both of resonant and broadband type are the most common used sensors in AE due their low cost, compactness (Wang et al., 2008) and easy installation procedure (Ozevin et al., 2006). Resonant type of transducers have relatively high displacement sensitivity, which is 10^{-13} m compared to broadband transducers, whose sensitivity is approximately 10^{-11} m (Godin et al., 2018). However, the resonant transducers detect a small range of frequency compared to broadband transducers (Scruby, 1987). Figure 3.11 shows frequency response function of both type of sensors. While the resonant sensor shows a narrow range of frequencies, between 0-50 kHz, in a more sensitive, broadband sensor shows wider range of frequency with more resonance frequencies.

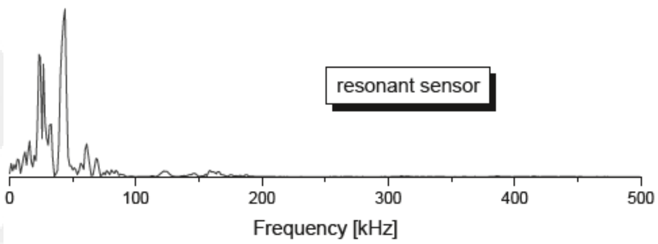

(a) Resonant sensor

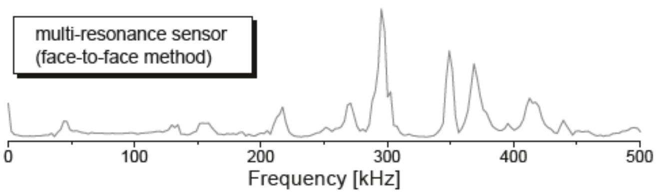

(b) Broadband sensor

Figure 3.11 Frequency response function of resonant and broadband sensors (Grosse & Ohtsu, 2008)

In this study PIC255, piezoelectric ceramic material based on modified lead zirconate titanate (PZT) is used as both sensor and actuator. According to manufacturer (PI Ceramic GmbH, nd) the related product is suitable for actuator applications for dynamic operating conditions in addition to using as a low-power ultrasonic transducer.

3.2.4 Acoustic Emission Data Analysis

3.2.4.1 Time-Domain Analysis

Mostly used time domain descriptors in literature are illustrated in Figure 3.12. These descriptors are defined by Godin et al. (2018) as:

- Event: Local material change giving rise to the acoustic emission.
- Amplitude: Corresponds to the signal peak value and is calculated from the amplitude V measured in Volts.

$$A[dB] = 20log(\frac{V}{V_{ref}}) + G \tag{3.6}$$

  where V_{ref} is equal to 1μV and G is preamplifier's gain.

- Arrival time: Time of the first threshold crossing.
- Rise time: Corresponds to the time between the first threshold crossing and the time of the maximum peak.
- Count: Number of time hits cross the threshold.
- Duration: Time difference between the first and last threshold crossing.
- Energy: Integral of the squared of signal voltage over the duration

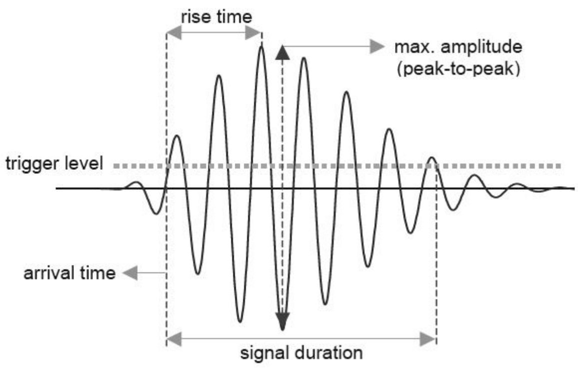

Figure 3.12 Typical AE time-domain parameters (Hellier, 2003)

In previous studies, analysis of AE measurements in time domain is used to relate different micro-mechanical damage mechanisms to specific amplitude values in composite materials (Berthelot & Rhazi, 1990; Barre & Benzeggagh, 1994). In particular, magnitude and energy are considered as important descriptors in amplitude-based analysis (Baccar, 2015). However, the results of some studies which used time domain parameters are contradictory, because of the particular failure modes are identified in different amplitude ranges for same materials (Gutkin et al., 2011). Ni & Iwamoto (2002) investigated the attenuation effect on both amplitude and frequency parameters and reported that while amplitudes of signal are affected by attenuation greatly with the increment of propagation length, frequencies of AE signals almost unchanged. Based on this information, authors suggested to use frequency domain parameters as a more reliable way to analysis of AE signal in composites.

3.2.4.2 Frequency-Domain Analysis

Due to limitations of amplitude-based analysis, many studies used frequency domain features to distinguish different damage modes in composite materials. The peak frequency is one of the most commonly used descriptor in frequency domain regarding damage identification. The frequency spectrum of recorded AE signals are obtained using algorithms such as Fast Fourier Transform (FFT). The studies also used time-frequency transforms to obtain peak frequencies with time resolution.

In Table 3.2, the summary of different studies which investigated the frequency content of different micro-mechanical damage modes is presented.

3.2.5 Signal Processing for Damage Detection

The signals can be represented in different domains in order to obtain more information about characteristics of the signal. Different representations of signals can be obtained by expanding the signal by set of functions (Cohen, 1995). In AE

Table 3.2 Summary of reported frequency ranges of damage modes (Wirtz, 2015)

Author	Matrix Crack	Debonding	Delamination	Fiber Breakage
Bussiba et al.	140 kHZ	300 kHz	-	405 kHz
Marec et al.	50-150 kHz	170-350 kHz	-	-
De Groot et al.	90-100 kHz	240-310 kHz	-	> 300 kHz
Suzuki et al.	30-150 kHz	180-290kHz	-	300-400 kHz
Baccar et al.	100-150 kHz	-	< 120 kHz	350-500 kHz
Bak et al.	30-150 kHz	130-220 kHz	-	> 300 kHz
Oskouei et al.	100-250 kHz	250-350 kHz	-	400-500 kHz
Hamdi et al.	30-170 kHz	180-290 kHz	30-90 kHz	300-420 kHz
Gutkin et al.	50 kHz	200-300 kHz	50-150 kHz	400-500 kHz
Bohse	100-350 kHz	-	-	350-700 kHz

analysis, the importance of frequency domain representation is demonstrated by many studies (Ni & Iwamoto, 2002; De Groot et al., 1995). In this section, frequency analysis and time-frequency analysis methods are presented.

3.2.5.1 Fourier Transform

The frequency content of continuous-time signal can be obtained by using Fourier transform. Fourier transform is based on the Fourier expansion, describing any arbitrary function can be represented by sum of the sinusoidal functions. If $x(t)$ is a periodic function and continuous in time, the frequency spectra of x(t) can be determined by using Fourier transform as follows (Cohen, 1995):

$$X(\omega) = \frac{1}{\sqrt{2\pi}} \int_{-\infty}^{\infty} x(t) e^{-jwt} dt. \tag{3.7}$$

Fourier transform can only be applied to continuous-time signals. However, experimental measurements are composed of series regularly spaced at time, which is called discrete-time signal. Discrete Fourier Transform (DFT) can be used to obtain discrete frequency components $X[k]$, $k = 0, ..., N-1$ from discrete-time signal $x[n]$,

$n = 0, ..., N-1$ as follows (Leis, 2011):

$$X[k] = \sum_{n=0}^{N-1} x[n]e^{-jn\omega_k}, \tag{3.8}$$

with

$$\omega_k = \frac{2\pi k}{N}, \tag{3.9}$$

where ω_k stands for frequency of kth sinusoid. Today, Fast Fourier Transform (FFT) is commonly used to obtain frequency content of discrete-time signal due to its efficiency on computational costs. In practice, the sampling frequency should be two times greater than the highest frequency component of the measured signal to avoid aliasing distortion in the spectra. Let the sampling frequency is f_s, then the maximum frequency that can be detected is $f_s/2$, which is called as Nyquist frequency (Newland, 2012).

Although the frequency content of signal can be obtained by using FFT, the information of when the frequency component occurs and the changes over time is not available in frequency spectra. In other words, time resolution is lost after using FFT. Since, damage related AE events causes non-stationary transient waves, examining the frequency content with time information enables more useful information about AE source, so the damage. In order to obtain time-frequency representation of the signal, time-frequency analysis methods such as Short Time Fourier Transform (STFT) or Wavelet Transform (WT) can be used.

3.2.5.2 Short Time Fourier Transform

STFT is a method to obtain time-frequency representation of signal by applying Fourier transform to parts of signal, which have equal lengths along the time axis.

In order to apply time-localized Fourier transform, moving window function $g(t)$, which is centred at time τ is used in this method. Fourier transform is performed for each particular τ on a signal $x(t)$ within the window. The spectrogram, which is obtained from STFT can be expressed as,

$$X_T(\tau, w) = \int_{-\infty}^{\infty} x(t)g(t)e^{-jwt}dt, \tag{3.10}$$

where X_T stands for spectrogram, which is obtained from all composed local spectra (Gao & Yan, 2010).

Different types of windows are used for particular applications to obtain accurate spectrogram. Gaussian window is designed for analyzing transient signals, whereas Hanning windows are applicable to narrow band, random signals. The chosen window function has significant influence on time-frequency resolutions of the analysis results. Furthermore, the method is limited due to trade-off between time and frequency resolution, which is based on uncertainty principle. According to uncertainty principle, in case of choosing small window size in time-domain leads to decrease in frequency resolution. On the other hand, choosing large windows decrease the time resolution, whereas it enables improved frequency resolution. In experimental measurements, generally the specific frequency of the measured signal is not known. Therefore, choosing appropriate window size is difficult to obtain accurate time-frequency representation (Gao & Yan, 2010).

3.2.5.3 Continous Wavelet Transform

In contrast to STFT, which uses the windows in fixed size, the wavelet transform employs variable window sizes in order to find frequency components of the signal. In this method, a base wavelet $\psi(t)$ is scaled and shifted to obtain a group of functions which are used for comparing with signal. The wavelet transform of signal $x(t)$ can be expressed as,

$$\psi_(s, \tau) = \frac{1}{\sqrt{s}} \int_{-\infty}^{\infty} x(t)\psi^*(\frac{t-\tau}{s})dt, \tag{3.11}$$

where $s > 0$ stands for scaling parameter, which determines the time and frequency resolution of the scale based wavelet $\psi(t - \frac{\tau}{s})$. Specific values of s are inversely proportional to the frequency. The symbol τ denotes the shifting parameter, which translates the scaled wavelet along the time axis. ψ^* stands for complex conjugate of the base wavelet $\psi(t)$. In practice, the CWT is applied to discrete-time signals using discrete values for s and τ (Gao & Yan, 2010).

The time and frequency resolution of the STFT and CWT is illustrated in Figure 3.13.

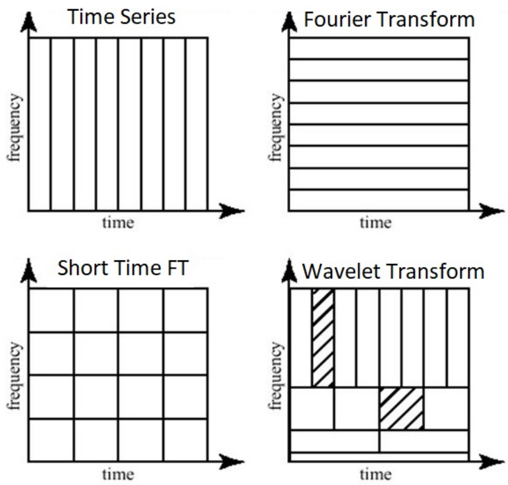

Figure 3.13 Time-frequency resolutions of STFT and CWT (Taspinar, 2018)

3.3 Artificial Neural Networks

3.3.1 Overview

Artificial neural network is a processor, consisting of simple processing units, which capable of storing information based on experience through its massively parallel distributed structure. Learning process enables neural network to acquire information from its environment. Furthermore, acquired knowledge is stored using synaptic weights which are inter-neuron connections. Both of the properties presented above show how neural network resembles the brain (Haykin, 1994).

Figure 3.14 shows a neural model. The fundamental operation of neural networks based on simple information processing unit, called as neuron. Weights represent the strengths of synapses or connecting links. A signal at the input of synapse *j*, is multiplied by the synaptic weight, ω_{kj} connected to neuron *k*. All of the input signals are added together after their weighting operations using linear combiner. Bias is a positive or negative scalar which increases or decreases the value of argument of activation function limiting the output of neuron (Haykin, 1994).

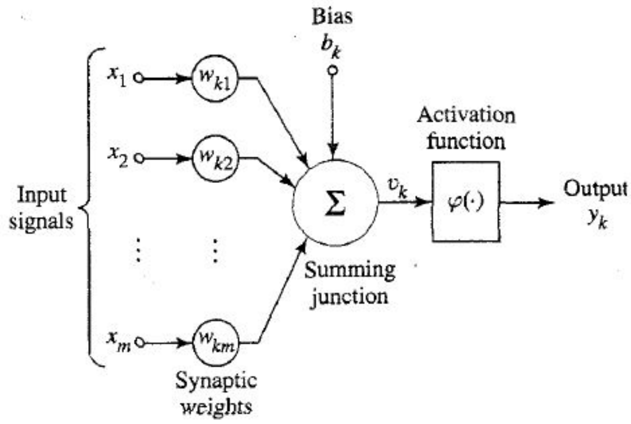

Figure 3.14 Nonlinear model of a neuron (Haykin, 1994)

The neuron k can be described as,

$$u_k = \sum_{j=1}^{m} \omega_{kj} x_j, \tag{3.12}$$

$$y_k = \phi(u_k + b_k), \tag{3.13}$$

where $x_1, x_2, ..., x_j$ are input signals; $\omega_{k1}, \omega_{k2}, ..., \omega_{km}$ are synaptic weights of neuron k; u_k is the linear combiner output due to input signals; b_k is the bias; $\phi(\cdot)$ is activation function; y_k is the output signal of neuron (Haykin, 1994).

Activation function applies non-linearity into the process of neuron (Charniak, 2019). There are different types of activation functions such as threshold function, sigmoid function or rectified linear function. Glorot et al. (2011) revealed that using rectified linear function yields better performance for training deep neural networks on supervised tasks compared to logistic sigmoid function or hyperbolic tangent function.

In neural networks, the neurons are generally organized in the form of layers. There are two kind of neural network, based on its structure: (i) single-layer neural network and (ii) multi-layer neural network. The structure of the both type of network is illustrated in Figure 3.15. Single-layer neural network, which is the simplest form of neural networks, consists of input layer of source nodes and output layer of neurons. Designation of "single" or "multi" refers to a number of output layer of computational nodes. Since the input layer of source nodes is not a computational layer, it does not contribute to the number of layers (Haykin, 1994).

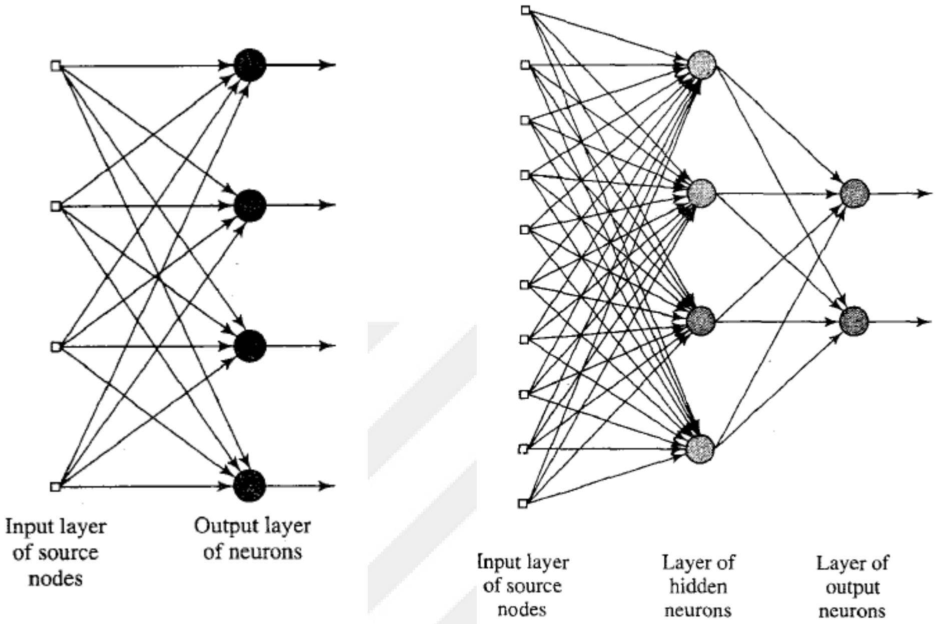

(a) Single-layer Neural Network

(b) Multi-Layer Neural Network

Figure 3.15 Neural Network structures (Haykin, 1994)

3.3.2 Deep Neural Networks

Deep neural networks are multi-layer neural networks, which have more than one hidden layer. According to LeCun et al. (2015), deep learning enables computational models, which are composed of multiple layers to learn representations of data. Deep learning applications are quite successful at image and speech recognition tasks, natural language processing and other domains such as medicals studies and genomics (Gu et al., 2018; LeCun et al., 2015). The method employs back-propagation algorithm to obtain how to change its internal parameters to compute the representations of large data sets by computing previous layer representations (LeCun et al., 2015).

The following information is based on the review of LeCun et al. (2015). In order to learn representations, the neural network uses a set of methods, which enables the network to take input as a raw data without any feature extraction. As a result, the representations which are needed for classification tasks are discovered automatically by the network. Deep learning methods are based on single, non-linear neuron which transforms the representations at one level into the representation at a higher and more abstract level by starting with input data. The network, which is composed of those neurons can learn very complex functions by composing enough transformations of those multiple representations. Representations of higher layers include dominant characteristics of input image, which can be used for identification whereas the unnecessary information within the image is not considered. For instance, if an image, which is in a form of array of pixels is an input for network, first layer of representation includes features such as presence or absence of edges at particular orientations and locations in the image whereas second layers typically detect the pattern by arranging those edges regardless of small variations in the edge positions. The third layer may assemble the patterns into larger combinations, which corresponds to the part of objects. Finally, subsequent layers detect objects by combining these parts. The significance of deep learning is that the feature layers are not designed by the engineers. The layers learn and modify themselves by learning from the data using a general-purpose learning procedure (LeCun et al., 2015).

3.3.2.1 Supervised Learning

The most of the machine learning and deep learning methods employ supervised learning (Kelleher, 2019; LeCun et al., 2015). In supervised learning related to image recognition task, the labelled or categorized images are shown to model during training and the model generates an output in a form of a vector which includes scores for each label or category. If the desired category has the highest score in this vector, it indicates that the category is classified successfully (LeCun et al., 2015). However, that unlikely happens before training. In training phase, the error, which is called as objective or error function, between the output and desired scores is computed. Then the network adjusts its internal parameters such as weights and biases to reduce this error. The weights and biases identify the input-output relation of the network. Typical deep learning system is composed of hundreds of millions of those weights (LeCun et al., 2015).

In order to adjust the weights, a gradient vector is computed for each weight during the learning. The gradient vector indicates the effect of small amount of increase in weight on error. The opposite direction to the gradient vector is used while adjusting the weights (LeCun et al., 2015).

The objective or error function, which is averaged on all training samples can be visualized as hilly landscape. The negative gradient vector shows the direction of the lowest altitude in this landscape. This lowest altitude is a place where the output error is minimized on average (LeCun et al., 2015).

One of the most common method to adjust weights is called Stochastic Gradient Descent (SGD). In SGD, the average gradient is computed for a few samples in training set and the machine adjusts the weights based on computed average gradient. The process is repeated until the average of the objective function stops decreasing (LeCun et al., 2015). The reason for the method is named as stochastic is that the computed gradient over a few samples gives a noisy estimation on average gradient over all samples. The computed weights based on this method are quite successful and quick in computation compared to more complex optimization techniques (LeCun et al., 2015). When the training process is finished, the performance of trained network is measured using another set of examples, called as training set. Using another set of examples shows the generalization ability of the model, which is an ability to show sensible performance on new inputs which are never seen during the training process.

3.3.2.2 Back Propagation

The computation of gradient of an objective function with respect to weights is possible by using backpropagation procedure, which is practical application of chain rule for derivatives. The main idea behind backpropagation is that computing gradient of error function with respect to input modules is possible by using computed gradient with respect to the output of the networks (LeCun et al., 2015).

Many applications of deep learning use feed-forward architecture, which takes an input in a fixed size such as an image and gives a fixed size of output such as probability of each of several category as illustrated in Figure 3.16a (LeCun et al., 2015). Single neuron takes its input from previous layer and computes the weighted sum and passes the result through a non linear function as follows,

$$z_k = \sum_{m=1}^{j} \omega_{jk} y_j, \quad \forall j \in H1. \tag{3.14}$$

In Equation 3.14, ω_{jk} stands for the weights collected at node k whereas y_j denotes the inputs to the same node. In order to calculate output non-linear function takes weighted sum as an argument as

$$y_k = f(z_k). \tag{3.15}$$

In Equation 3.15, $f(.)$ represents the non-linear function. The recently, the most popular non-linear function is rectified linear unit (ReLU), which is simply the half-wave rectifier. In past decades sigmoid functions such as tangent hyperbolic are used commonly. However, the ReLu learns much faster in the networks with many layers, which allows training deep networks without unsupervised pre-training (LeCun et al., 2015).

In backward passing error derivative with respect to the output of each unit should be calculated to find gradient. Figure 3.16 illustrates the forward and backward equations for each layer in a network composed of two hidden layer.

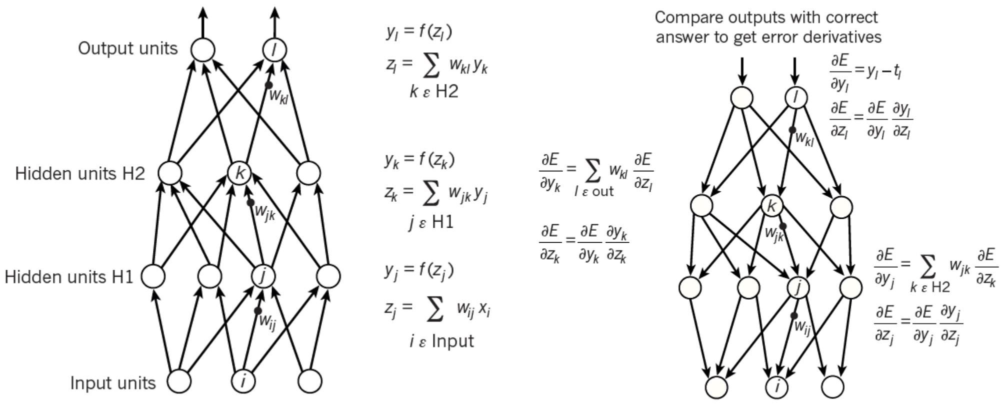

(a) Forward (b) Backward

Figure 3.16 Forward and backward passing in Deep Network (LeCun et al., 2015)

3.3.3 Convolutional Neural Networks

Convolutional Neural Network (CNN) is a specific type of deep learning architecture, inspired by living creatures visual perception system, taking images as an input. The visual cortex of animals consists of cells which are capable of detecting light only on its own receptive field. The first neural network model based on this analogy is proposed by Fukushima & Miyake (1982), which is regarded as predecessor of modern CNN architecture (Gu et al., 2018). Theoretical framework of modern CNN is established by LeCun et al. (1990) as applying back-propagation learning algorithm to train multi-layer neural network, which is called as LeNet-5, whose task was classifying handwritten digits. LeNet-5 achieved this task by obtaining important representations of images and using this information to be able to recognize patterns in row input images. In 2008, AlexNet, which is classical CNN architecture is proposed by Krizhevsky et al. (2012), performed important improvement on image classification task compared to previous methods. Although general architecture of ALexNet is similar to LeNet5, the number of layers of AlexNet was greater compared to LeNet-5, indicating the effect of deep structure of AlexNet on its performance. After the achievement of ALexNet, many network structure is introduced such as ZFNet, VGGNet, GoogleNet and ResNet to improve AlexNet performance and the main trend of these networks was changing the architecture deeper (Gu et al., 2018). Although the deeper structure in networks leads to better approximation to target function and increased ability to extract feature representations of images, it also increases the complexity of the network which causes to optimization problems and also overfitting (Gu et al., 2018).

Unlike regular neural networks, layers of CNN have three dimensions in which the neurons are arranged: width, height and depth as it is illustrated in Fig 3.17. Every layer of CNN takes 3D input volume and transforms that into 3D output volume. Furthermore, the neurons are not connected to all other neurons arranged in previous layer like regular neural networks.

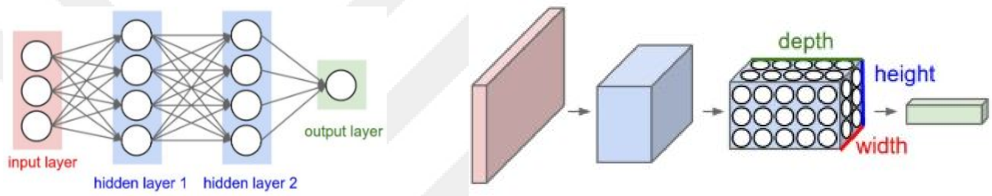

(a) Regular 3-layer Neural Network

(b) Conceptual design of CNN layers

Figure 3.17 Regular Neural Networks and Convolutional Neural Networks (Stanford, 2019)

Despite the many slight differences in CNN architectures released in literature, the main components of these architectures are similar. There are 2 types of basic layers in CNN architectures: (i) Convolutional layer and (ii) Pooling layer. Figure 3.18 shows the architecture of LeNet-5, famous classical CNN architecture for digit recognition task, which is composed of basic CNN components.

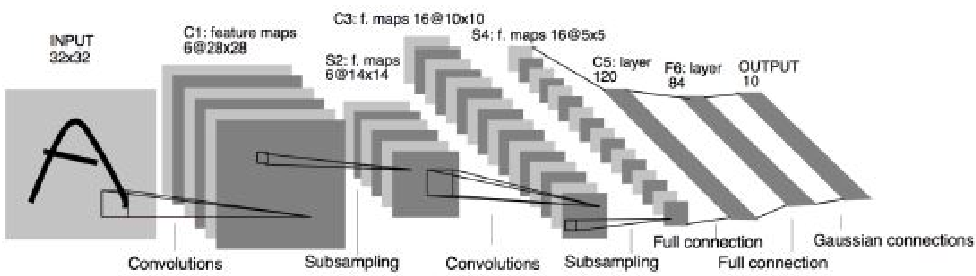

Figure 3.18 Architecture of LeNet-5 (LeCun et al., 1990)

3.3.3.1 Convolutional Layer

The convolutional layer consists of a number of convolution kernels or filters which are used to obtain different feature representations of images. For instance, one of the kernels in convolution layer of trained network might look for specific type of edge in an input image, whereas one of the other kernel look for individual curve in the same input image. The operation is based on convolving the input image with learned kernel or filter which generates feature map as illustrated in Figure 3.19.

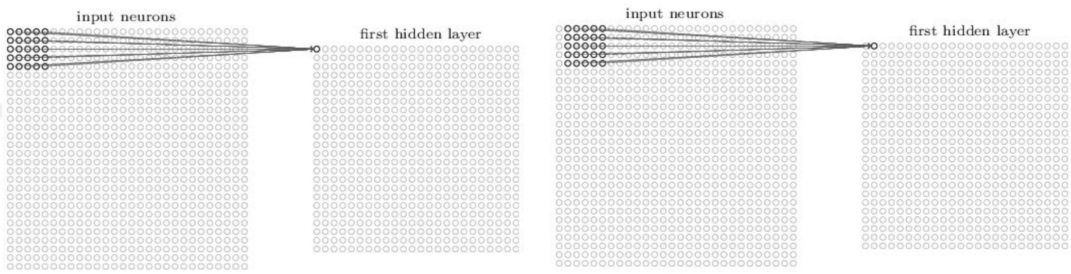

(a) First position of convolution filter　　(b) The filter is slided one pixel right over the input image

Figure 3.19 Visualization of 5x5 convolving filter on input image (Nielsen, 2015)

Height and width of the feature map depends on filter size and input image size, whereas depth of feature map depends on number of filters used in convolutional layer. LeNet-5 uses 6 filters of size (5x5) in its first convolutional layer. Therefore, first feature map of the architecture is composed of 6 layers as it is illustrated in Fig.3.18.

Every individual neuron of feature map are connected to a local area of previous layer which is called as receptive field and the size of receptive field is the same as the size of convolutional filters or kernels. Mathematically, the feature value at location (i, j) in the kth feature map of lth layer, $z^l_{i,j,k}$ is calculated by Gu et al. (2018) as follows:

$$z^l_{i,j,k} = \boldsymbol{W}^{l\,T}_k \boldsymbol{x}^l_{i,j} + b^l_k, \tag{3.16}$$

where $\boldsymbol{W}^l_k$ and b^l_k denotes for weight vector and bias term of the kth filter of the lth layer respectively. $\boldsymbol{x}^l_{i,j}$ stands for the input vector which is composed of elements located at the receptive field of the neuron located at (i, j) of the lth layer. It should be noted that $\boldsymbol{W}^l_k$ is the common weight factor for the all neurons located at same depth slice of the feature map $z^l_{:,:,k}$, meaning that the same feature is looked for in a different areas of input image using convolution operation. Sharing the same weight parameters dramatically reduce the number of parameters in a model and therefore reduce the computational cost. The non-linearity of the model is introduced by using activation functions. The activation value of feature map $z^l_{:,:,k}$ can be calculated by Gu et al. (2018) as follows:

$$a^l_{i,j,k} = a(z^l_{i,j,k}). \tag{3.17}$$

3.3.3.2 Pooling Layer

The pooling layer, which is generally placed between two convolutional layer, aims to reduce spatial dimension of feature map. Reducing the size of feature maps provides efficiency in computational costs since it leads to decrease in number of parameters which is going to be calculated by network. Furthermore, it also controls overfitting (Stanford, 2019). The pooling operation can be described for each feature map $a^l_{:,:,k}$ as follows (Gu et al., 2018):

$$y^l_{i,j,k} = pool(a^l_{m,n,k}), \quad \forall (m,n) \in \mathcal{R}_{ij}, \tag{3.18}$$

where $\mathcal{R}_{ij}$ denotes the local neighbourhood around the location (i,j). Pooling layers can perform different functions such as max pooling, average pooling or L2-norm pooling. The most commonly used pooling layer is max pooling due to its satisfying performance in recent applications, whereas the average pooling was used frequently in the past (Stanford, 2019).

Another optional layers is fully connected layer consists of neurons which have full connections to all activations in previous layer. It gives final probabilities for each labels.

CHAPTER FOUR
EXPERIMENT

The aim of this study is to investigate the usage of CNN while classifying AE measurements in order to distinguish different micro-mechanical damage modes in composites. Furthermore, the evaluation of propagation effects on the classification performance of CNN model is addressed. The experiment is designed to address highlighted objectives. Experimental setup, whose details are given in the next section, contains Carbon Fiber Reinforced Polymer (CFRP) plate and Piezoelectric Wafer Active Sensor (PWAS). The CFRP plate is the structure on which the measurements are performed. The PWAS is used both as an actuator to excite particular Lamb wave modes, and as a sensor to measure those waveforms. Furthermore, a waveform generator is used to excite the PWAS and a data acquisition system is used to digitize the measured waveforms. Different types of damage modes are represented by dominant fundamental Lamb wave modes triggered by the PWAS. The measurements are taken with sensors mounted at different distances to the AE source to address the propagation effects such as attenuation and dispersion on classification performance.

4.1 Experimental Framework

In this section, experimental framework is given in details to provide information for future works. In order to establish repeatability, same experimental procedures need to be followed.

The measurements are performed on a unidirectional, single layer CFRP plate with 45° fiber orientation angle and dimensions $800 \times 800 \times 1\,mm^3$ as illustrated in Figure 4.1. The width and height of the specimen is chosen such that the reflection effects on the measured signal are avoided. The plate is hanged by two adhesive tapes to satisfy the free boundary conditions. Also, in order to increase the signal-to-noise ratio, the plate is grounded by connecting the edge of the plate to the oscilloscope ground terminal through a conductor.

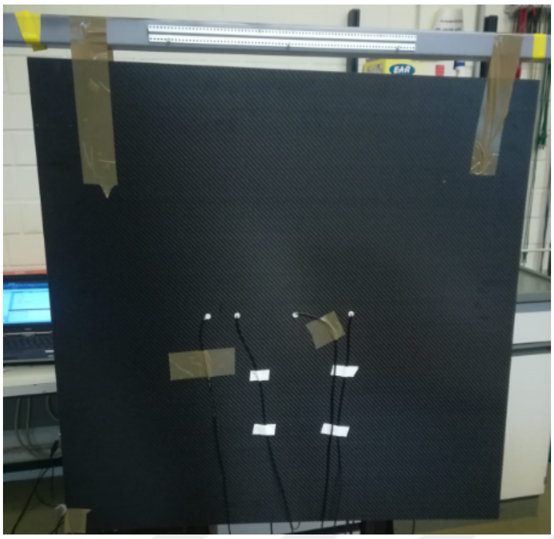

Figure 4.1 CFRP plate on which measurements are performed (Personal archive, 2020)

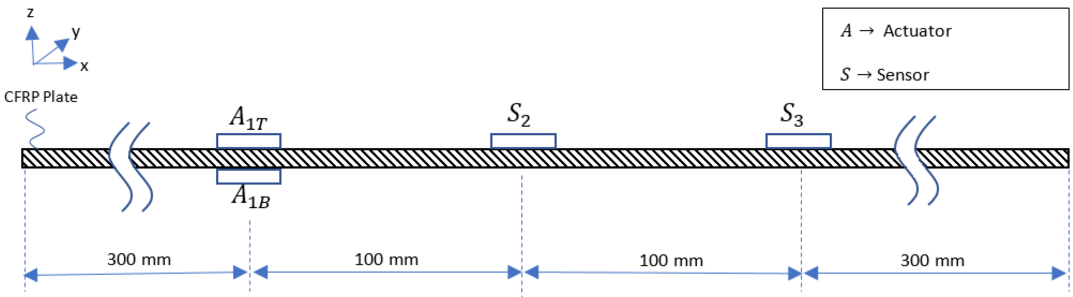

Figure 4.2 CFRP plate with PWAS configuration

Disc shaped PWASs with 10mm diameter and 0.55mm thickness are used both as an actuator and as a sensor. PWASs are mounted to the surface using cyanoacrylic adhesive. It should be noted that direction of propagation path of the emitted waveform has influence on measured signal as fiber orientation is in one direction on CFRP plate. Therefore, the PWASs are mounted in only x direction, which satisfies 45° between propagation path and fiber orientation of plate in this study. In order to trigger particular damage modes, PWASs are mounted the same point, A at both upper surface A_{1T} and bottom surface A_{1B} of plate as illustrated in Figure 4.2. The generated waveforms are measured by PWASs mounted at S_2 and S_3. The PWAS actuators are excited by using Keysight 33500B signal generator. The excitation signals are designed using Matlab software which is installed on a computer connected to the waveform generator via USB. In order to repeat the measurements,

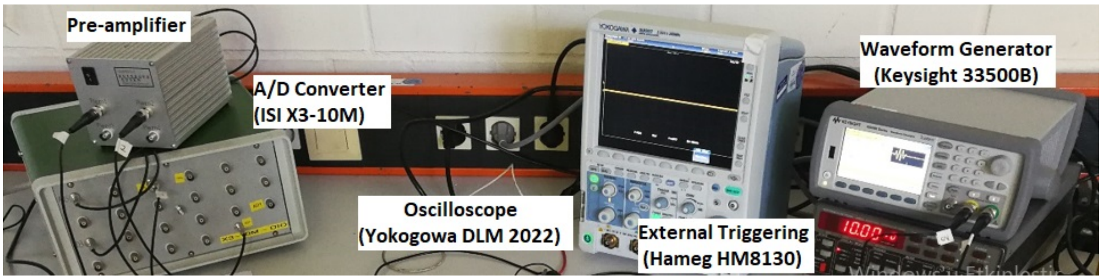

Figure 4.3 The measurement chain (Personal archive, 2020)

the signal generator is triggered with external triggering with a frequency of 10Hz. This triggering signal is recorded with using different channels in A/D converter (X3-10M) in order to use triggering information on splitting process of measurements. The hardwares used in triggering and measurement chain are illustrated in Figure 4.3.

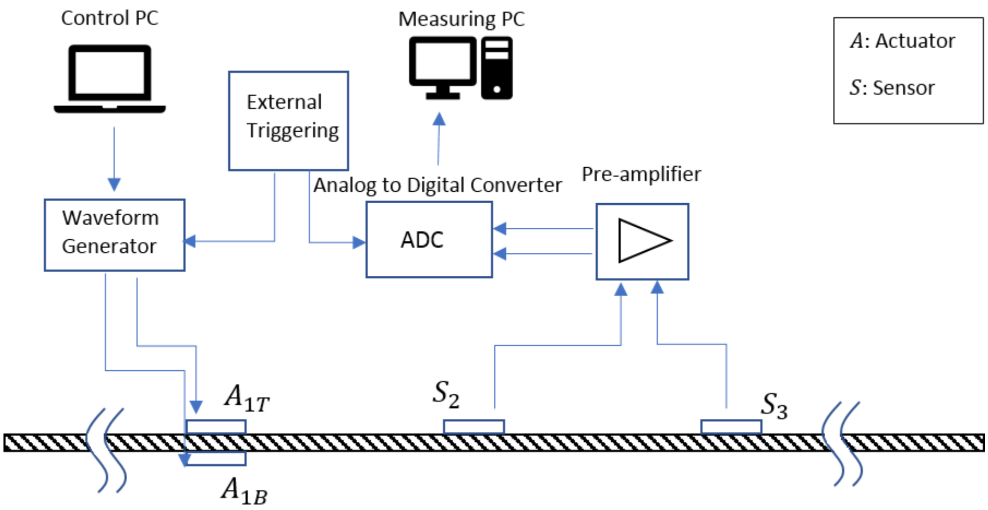

Figure 4.4 Experimental setup

The schematic diagram of the experimental setup is shown in Fig.4.4. The generated waveforms are measured by highly sensitive piezoelectric transducers and those measurements are amplified before getting digitized by the A/D converter. The digitized measurements are stored in the measuring PC for further post-processing, which includes applying Continuous Wavelet Transform (CWT) and establishes Convolutional Neural Network (CNN) models to classify those measurements.

4.1.1 Artificial Source Generation

In plate like structures, elastic waves propagate in the form of fundamental Lamb wave modes, symmetrical (S_0) and asymmetrical (A_0). The studies related to modal AE have shown that micro-mechanical damage modes in composites can be distinguished according to their modal content (Eaton et al., 2011; Gorman, 1991). For instance, while the delamination occurs, the physical behaviour of the structure is characterized by micro displacements in a direction of out of plane, so the A_0 modes are dominant in a measured waveform. In contrast, matrix cracking and fiber breakage is dominated by symmetrical modes because the both of the failure creates micro-displacements inside the plane. Based on this information, different damage modes are represented by fundamental Lamb wave modes in this experiment.

The methods used in this study to stimulate particular Lamb modes are based on Su's study (Su & Ye, 2009). Different Lamb modes can be stimulated using techniques, which are called wave-mode tuning. In an experimental guided wave, activating pure Lamb modes is quite easy by using ultrasonic probes, whereas triggering a pure individual Lamb mode is not possible using PWASs. The PWASs which are mounted on the structure generate both symmetrical and asymmetrical modes simultaneously. Therefore, the resulting waveform is superimposed by both symmetrical and asymmetrical modes. However, the particular wave modes can be enhanced while the minimizing other undesired modes using specific PWAS configurations and exciting in a specific way. If two PWAS are mounted at same planar coordinates at both upper and lower surface of plate, the desired modes can be stimulated as follows: when the both PWAS are energized in-phase, the resulting signal is dominated by S_0 mode, whereas A_0 mode becomes dominant in resulting signal if the both PWAS is energized in out-of-phase, which indicates 180° phase delay. In addition to specific PWAS configuration and synchronization, the waveforms which are used to excite PWAS actuators have an important role to stimulate pure Lamb modes. According to Su & Ye (2009), the narrowband signals with a certain number of cycles show satisfying performance to avoid wave

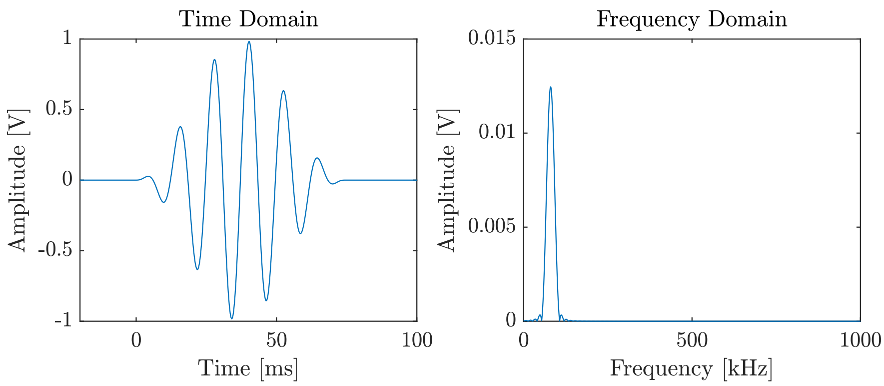

Figure 4.5 Waveform used for exciting PWAS: Burst signal with 6 cycles

dispersion. In practice, windowed tone bursts are most commonly used waveforms for exciting particular Lamb modes. The effect of using windowing on excitation signal is to narrow the bandwidth of the signal. Furthermore, number of cycles of burst signal has an effect on bandwidth of the waveform. Increase of cycles of burst signal also narrows the bandwidth and decreases the dispersion. However, long duration of signal allows to overlaps between reflected waves and excited waveform. In this experiment, burst signal, which is illustrated in Figure 4.5, windowed by hanning function, with 6 cycles and 100kHz center frequency is used.

The waveforms dominated by symmetrical or asymmetrical modes, representing different micro-mechanical damage modes are generated using PWAS couple with method mentioned above. In order to provide variety of damage, dominant wave modes are generated in different amplitudes and generated waveforms are categorized into different amplitudes of dominant symmetric and asymmetric modes. Consequently, 10 different amplitude dominant S_0 and 10 different amplitude of dominant A_0 waveforms are generated. The measurements are repeated 100 times for each waveform to obtain enough training data for CNN model.

In order to examine modal content of generated waveforms, same PWAS configuration, which is used for exciting particular Lamb wave modes can be used as a sensor couple. The superposition of measured signals from top and bottom sensor indicates the symmetric mode content, whereas the difference of the signals indicates the asymmetric mode content (Chen, 2007). Based on this information, additional

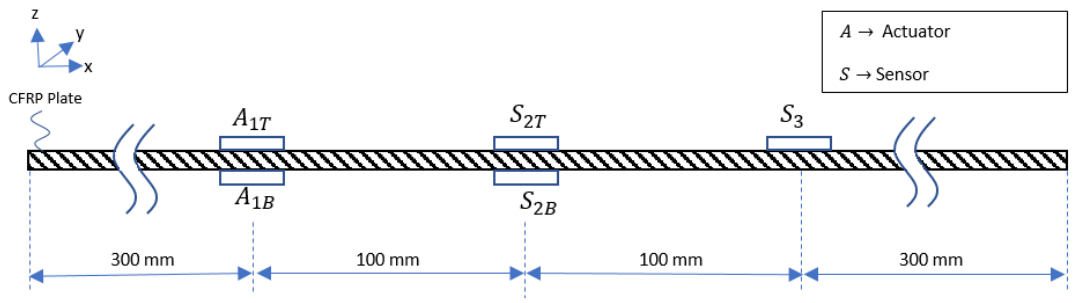

Figure 4.6 PWAS configuration to examine modal content of generated waveforms

PWAS is mounted at bottom surface of plate at same planar coordinates with S_{2T} as illustrated in Figure 4.6.

Two of the generated waveforms, which are dominated by highest amplitude symmetric mode (S_0) and highest amplitude asymmetric mode (A_0) are measured by using S_{2T} and S_{2B} sensors. The modal content of the generated waveforms are determined by using the method mentioned above and illustrated in Fig. 4.7 and Fig. 4.8 respectively.

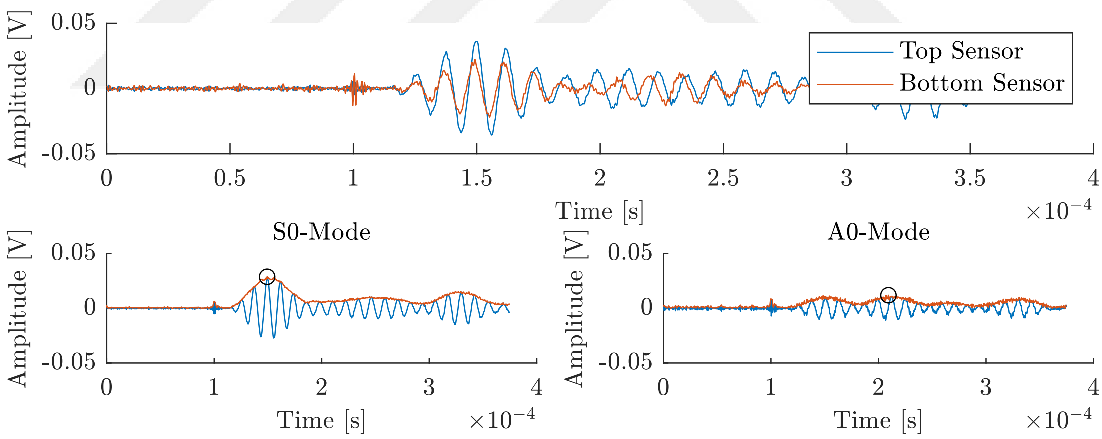

Figure 4.7 Generated waveform dominated by highest amplitude symmetrical mode

4.2 Classification of AE measurements by CNN Models

4.2.1 Pre-processing and Evaluation of Input Data

Deep learning is data driven approach which eliminates manual feature extraction from data or signals. The model determines features which are going to be considered

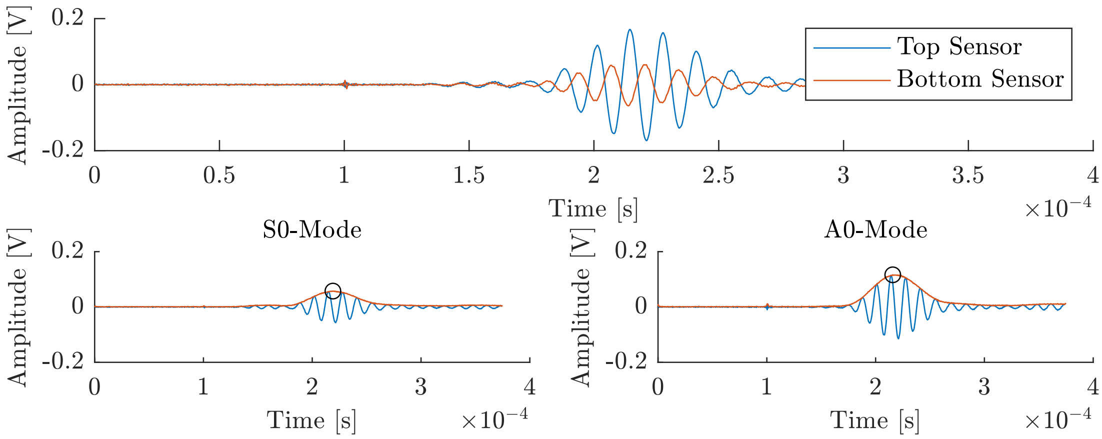

Figure 4.8 Generated waveform dominated by highest amplitude asymmetrical mode

as an important parameter in classification task during the learning process with labelled data. Therefore, deep learning models generally use raw signals as an input without feature extraction (Ebrahimkhanlou & Salamone, 2018).

4.2.1.1 Pre-processing of Input Data

In this study, Convolutional Neural Networks (CNN), specific deep network architecture using the images as an input, is used to classify AE measurements. The measurements, which consist of 10 different amplitude dominant symmetric mode (S_0) and 10 different amplitude dominant asymmetric mode (A_0) are transferred into time-frequency domain using Continuous Wavelet Transform (CWT) in order to enhance multimodal and dispersive characteristic of waveforms (Ebrahimkhanlou & Salamone, 2018). The absolute value of wavelet coefficients is normalized to create input images, with size 227x227x3 using Matlab code in Appendix 1. The size of input images is chosen based on the aim of using the same dataset for fine-tuning specific type of CNN architecture, AlexNet, which uses input images in size of 277x227x3. Figure 4.9 shows the images, which include one sample for each generated AE source, created using the measurements of S_2. In Figure 4.9, first two row consist of images which represent waveforms dominated by symmetrical modes, whereas third and fourth row consist of images representing waveforms dominated by symmetrical modes. Top left image and bottom right image represents the waveforms

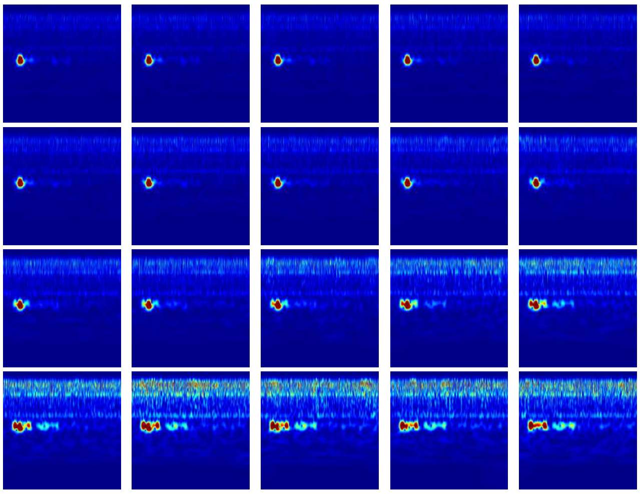

Figure 4.9 Input images for CNN: Time-frequency representation of waveforms measured by S_2

dominated by highest amplitude symmetrical mode and highest amplitude asymmetrical mode respectively. In this arrangement of images, the effect of symmetrical mode increases in the images in a direction of right and down, while the asymmetrical mode domination decreases. The images which are created using

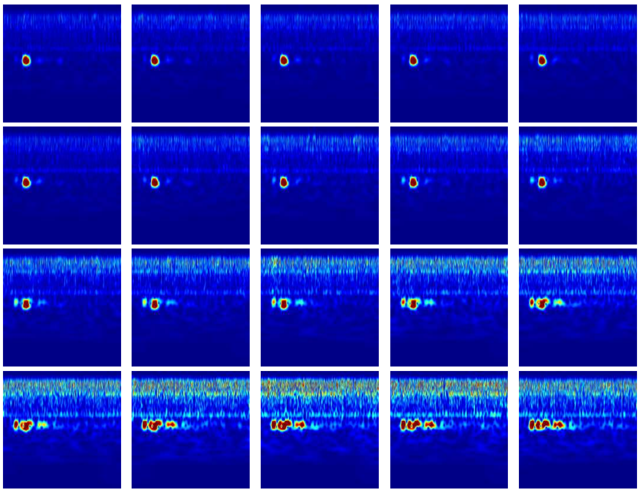

Figure 4.10 Input images for CNN: Time-frequency representation of waveforms measured by S_3

measurements obtained from S_3, which is the sensor mounted at long distance to AE source is illustrated in Figure 4.10 using same arrangement procedure.

4.2.1.2 Evaluation of S_2 and S_3 Measurements

The time-frequency representation of the waveform dominated by highest amplitude symmetrical mode and highest amplitude asymmetrical mode are illustrated in Figure 4.11.

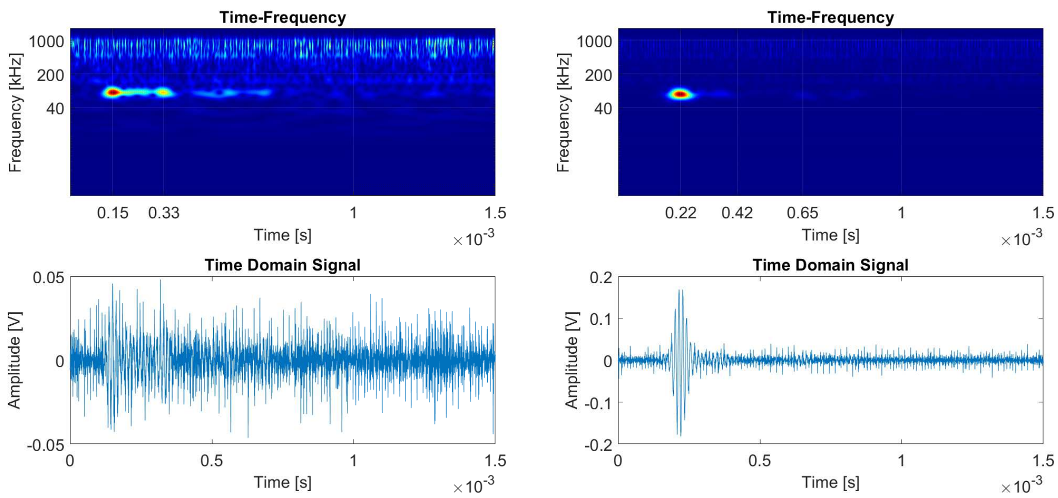

(a) Waveform dominated by symmetric mode (b) Waveform dominated by asymmetric mode

Figure 4.11 Time-frequency domain representation of waveforms measured by S_2

In time domain representation, distinguishing the waveform from the noise is difficult in a measurement dominated by symmetrical mode in Fig.4.11a, whereas the burst signal is clearly observed in a measurement which is dominated by asymmetrical mode Fig.4.11b.

This can be explained by the nature of the fundamental wave modes. The measurements obtained from sensors, mounted on plate surface is more sensitive to out-of-plane displacements. Therefore, symmetrical modes are characterized by low amplitudes compared to asymmetrical modes in surface measurements. In time-frequency domain, center frequency of burst signal, 80 kHz, is clearly visible in both Fig.4.11a and Fig.4.11b. However, Figure 4.11a shows second peak at 0.33 ms and center frequency is visible in period of time between first peak and second peak. This can be explained by dispersion phenomenon and mode separation. The velocity of the fundamental wave modes is dependant on frequency and defined by dispersion

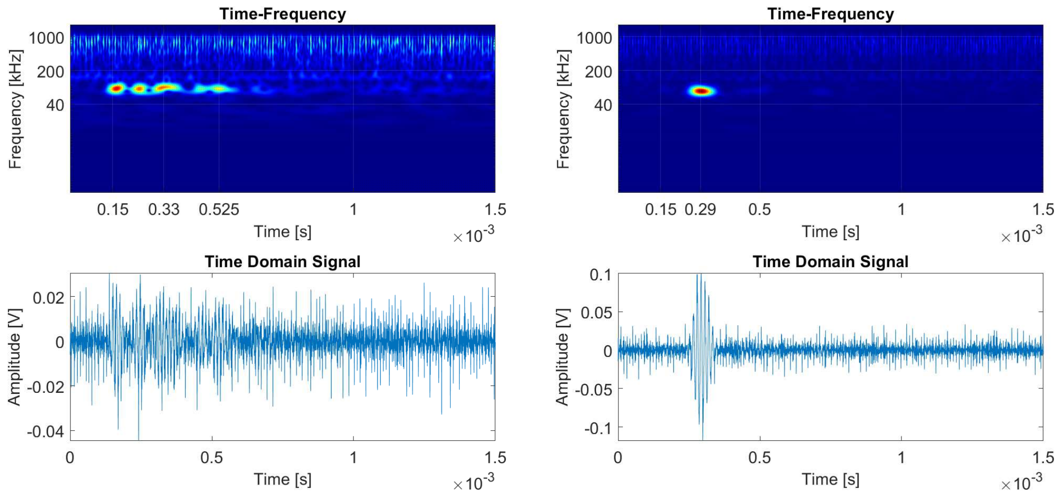

(a) Waveform dominated by symmetric mode

(b) Waveform dominated by asymmetric mode

Figure 4.12 Time-frequency domain representation of waveforms measured by S_3

curves as explained in Chapter 3.2.2. In particular, symmetrical wave modes have high velocities compared to asymmetrical modes at low frequencies. The mode separation due to velocity dispersion observed in Fig.4.11a is not visible on the measurement dominated by asymmetrical mode in Fig.4.11b. Moreover, the effect of high frequency noise is more visible on symmetrical mode due to low amplitudes of symmetrical mode. In other words, effect of noise seems as contrast in 2D image representation while it seems as signal-noise mix in time domain representation.

Figure 4.12 illustrates the time-frequency representations of signals measured by S_3, the sensor mounted at long distance to AE source. Time domain representations in Fig.4.12a and Fig.4.12b show the decrease in the amplitude of measured signals compared to S_2 measurements due to attenuation effects. Moreover, the mode separation in measured waveform dominated by symmetrical mode in Fig.4.12a is completely visible between 0.15 ms and 0.525 ms due to long propagation distance. The mode seperation could not be observed on the waveform dominated by asymmetrical mode like S_2 measurement.

4.2.2 Architectures of CNN Models

In this study, two different CNN model is used to classify AE measurements and performance of models is compared by using classification accuracies of both models. The first model, whose architecture is illustrated in Fig. 4.13 is created from scratch based on the reference studies (Ebrahimkhanlou & Salamone, 2018; Tabian et al., 2019) using Matlab code in Appendix 2. These studies use images of time-frequency representations as an input to CNN model in context of AE as well as the present study. The second model is pre-trained AlexNet which is fine-tuned by using transfer learning based on the learned features of the pre-trained model. The Matlab code in Appendix 3 is used to establish the new network in another domain. In this study, the term *proposed network* refers to the model created from scratch, whereas *AlexNet* will be used to refer fine-tuned AlexNet.

4.2.2.1 Proposed Model

The proposed model consists of three convolutional layers and two maximum pooling layers as illustrated in Figure 4.13. The batch normalization layers are used to reduce training time of the network. Also, this type of layer acts as a regularizer to avoid overfitting problem (Ioffe & Szegedy, 2015). Furthermore, dropout layers are added to architecture to prevent overfitting (Srivastava et al., 2014).

In order to fit convolutional filters or kernels, size of 3x3, over the input images and feature maps, the zero pixels are padded in the four directions of images. Therefore, width and height of the feature maps of convolutional layers remain same as the width and height of their inputs. However, the depth of the feature maps increases due to the increase of number of convolutional filters used in the network. The first convolutional layer, composed of 8 different convolutional kernels, leads to increase of depth of feature maps from 1 to 8. After a convolution operation of second and third convolutional layers, which are composed of 16 and 32 convolutional kernels respectively, the depth of feature maps reaches to 32. The non-linear character

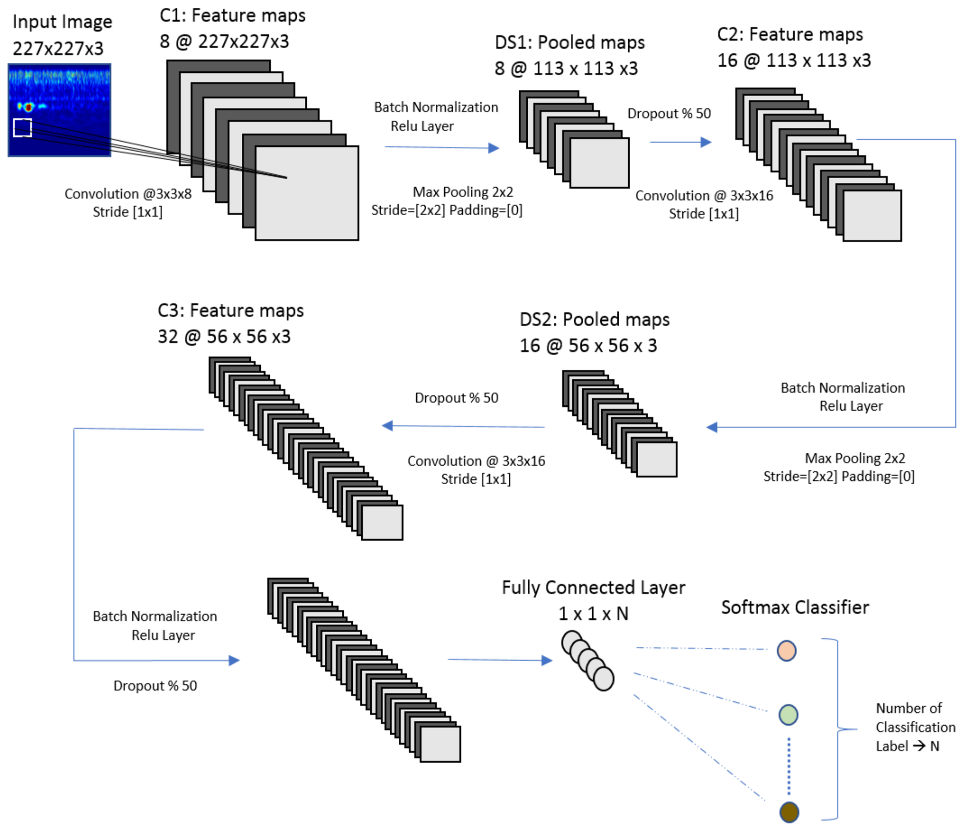

Figure 4.13 Architecture of proposed CNN model

of the architecture is provided using ReLu function as an activation function in the convolutional layer. Moreover, softmax layer and down-sampling operation applied on max-pooling layer contribute non-linearity characteristic to the architecture (Ebrahimkhanlou & Salamone, 2018).

Max-pooling layers are used for down-sampling the spatial sizes of images. The width and height of the images are reduced by half after down sampling by using 2x2 strides. However, the depth of the images remains same after down-sampling operation. In last layer, fully connected layer reduces spatial dimension into unity (1x1) while the depth of the fully connected layer becomes equal to the number of classification labels. The activations of neurons in the fully connected layer are evaluated by softmax layer by using softmax function to obtain probability of assigning input image to individual class label.

4.2.2.2 AlexNet

In order to compare and validate classification results provided from proposed model, the second model which is pre-trained network AlexNet is used in this study. Pre-trained networks are the networks trained on base dataset and used for target classification tasks and dataset after applying additional training process which is called fine-tuning (Yosinski et al., 2014). The method based on using pre-defined network in different classification task is known as transfer learning and specifically useful when the target dataset is insufficient to train large network because of the overfitting problem (Yosinski et al., 2014).

The architecture of AlexNet is illustrated in Figure 4.14. The network composed of 5 convolutional layer and 3 fully connected layer in addition to max-pooling and dropout layers. Furthermore, the layers are categorized into 2 part to train the model on two different GPU to be able reduce computational costs. The model is trained by using subdataset of ImageNet, which is high resolution RGB images which consisting of one thousand different category (Krizhevsky et al., 2012). Even though the images on which AlexNet is trained are different type of images compared to wavelet images, the present study used pre-trained AlexNet based on fact that the low level features of natural images and wavelet images such as such as edges, curves and color blobs are common, therefore these features can also be used to distinguish wavelet images.

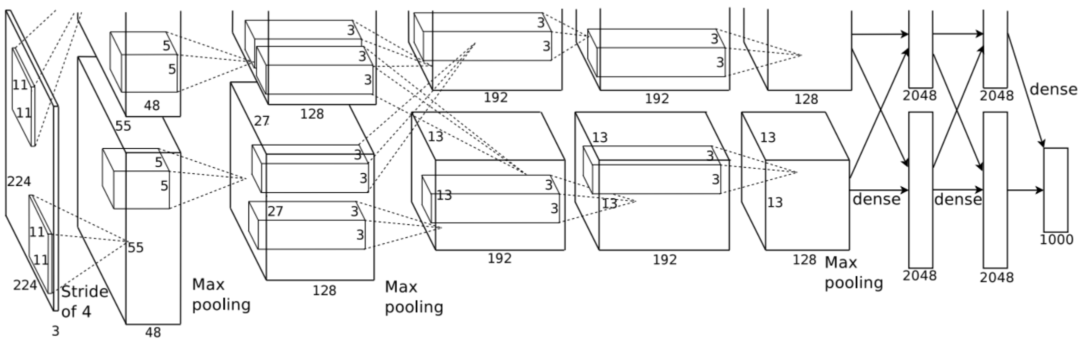

Figure 4.14 Architecture of AlexNet (Krizhevsky et al., 2012)

In order to use pre-trained AlexNet, all layers of the trained network are transferred into new network except from last three layers. Three additional layers;

fully connected layer, softmax layer and classification layer, are added to the transferred layers according to classification task of present study. In order to prevent considerable changes in the weight and bias parameters of transferred layers during the training process with new training data, learning rate factor is increased for fully connected layer whereas the default parameter is used for learning rate in other layers. Therefore, the new layers learn faster than transferred layers which prevent significant change in learned weights and biases.

4.2.3 Training Data and Classification Tasks

In this study, wavelet transform images of AE measurements dominated by different amplitude fundamental wave modes, which are illustrated in Fig.4.9 and Fig.4.10, are used as training data. Two set of images, which are taken from two sensors mounted at different distances to AE source are used to train individual network in a two different way by arranging the training data according to two different classification scenarios. First classification scenario includes two classification labels: symmetric mode and asymmetric mode. The measurements dominated by different amplitude symmetric modes and asymmetric modes in Fig.4.9 and Fig.4.10 are arranged to form labels *symmetric mode* and *asymmetric mode*. The second classification scenario includes 4 classification labels as considering amplitudes of the waveforms. In this scenario, the measurements are arranged into labels as *high amplitude symmetric mode*, *low amplitude symmetric mode*, *high amplitude asymmetric mode* and *low amplitude asymmetric mode*.

The both network used in this study, AlexNet and proposed network, are trained on training data, which is arranged according to classification scenarios. The trained networks are tested on testing data, which had been separated from training data before the training process. It should be noted that using different ratios between the training and testing datasets leads differences on the classification results. Therefore, splitting the limited data into training and testing sets is a compromise. However, the training and testing data was not limited in the present study, as a result of using artificial source to generate samples. In this study CNN networks are trained by using 300 samples and training process is monitored by using validation set, which consist of 100 samples. Finally, the models are tested on training sets, which consists of 100 samples for first classification scenario and 200 samples for second classification scenario. Furthermore, in order to increase repeatability of classification results, the present study avoid to use random data splitting.

In addition to testing the trained networks with the images of the particular sensor measurements which are used in training phase of networks, the networks are also tested on the images of another sensor measurements to address the propagation effects on classification performance.

CHAPTER FIVE

RESULTS

5.1 Classification into 2 Label: Symmetric and Asymmetric

5.1.1 Regular Testing: Training and Testing on Same Sensor Data

AlexNet

($n_{Training}$=300, $n_{validation}$=100, $n_{testing}$=100)

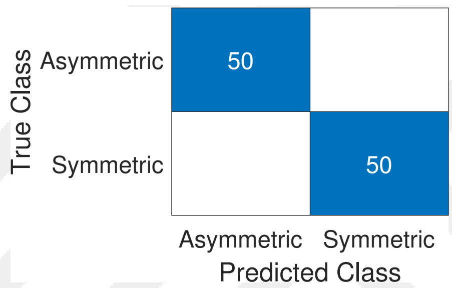

Figure 5.1 Confusion matrix of AlexNet: Trained and tested on S_2 measurements

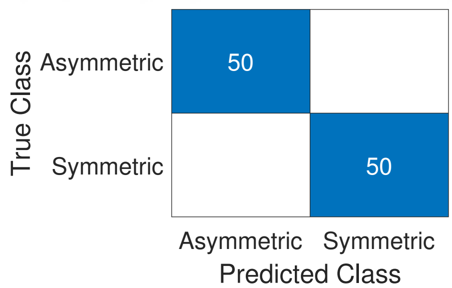

Figure 5.2 Confusion matrix of AlexNet: Trained and tested on S_3 measurements

Pre-trained AlexNet is tested on measurements of the sensor on which the networks are fine-tuned. Both S_2 and S_3 images are classified with 100% accuracy as illustrated in Fig.5.1 and Fig.5.2, which indicates the classification task is relatively easy for network.

Proposed Network

($n_{Training}$=300, $n_{validation}$=100, $n_{testing}$=100)

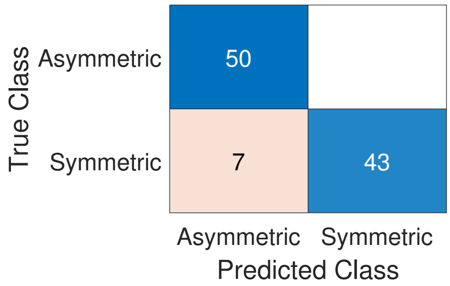

Figure 5.3 Confusion matrix of the proposed network: Trained and tested on S_2 measurements

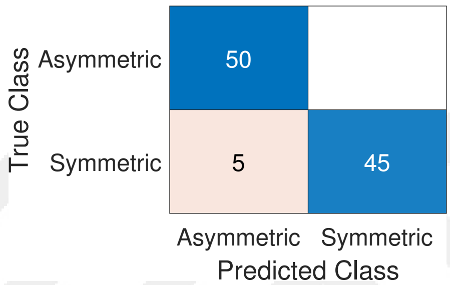

Figure 5.4 Confusion matrix of the proposed network: Trained and tested on S_3 measurements

The performance of the proposed network on classifying the data on which the network is trained is illustrated in Fig.5.3 and Fig.5.4. The classification accuracies are close to each other for both cases as 93% and 95%, respectively. After examining the misclassified images on both cases, it is observed that misclassified measurements are the waveforms dominated by lowest amplitude symmetric modes. The training data consist of different amplitude symmetric and asymmetric modes as illustrated in Fig.4.9 and Fig.4.10. The waveforms of lowest amplitude asymmetrical mode and lowest amplitude symmetrical mode are quite similar and represent border for labels. Therefore, it is expected to see misclassified samples especially on those samples. Furthermore, the results show that the performance of the proposed network is lower than classification performance of AlexNet on same classification task.

5.1.2 *Cross-Testing: Training and Testing on Different Sensor Data*

AlexNet

($n_{Training}$=300, $n_{validation}$=100, $n_{testing}$=100)

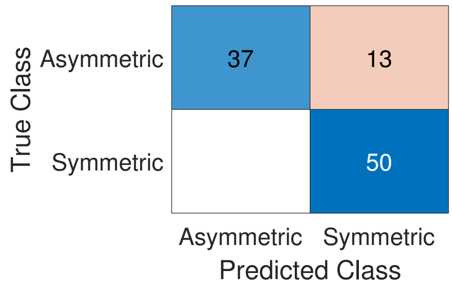

Figure 5.5 Confusion matrix of AlexNet: Trained on S_2 and tested on S_3 measurements

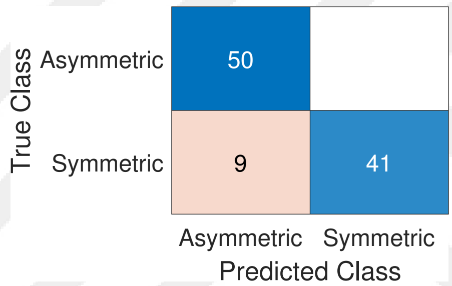

Figure 5.6 Confusion matrix of AlexNet: Trained on S_3 and tested on S_2 measurements

Fig.5.5 and Fig.5.6 show the confusion matrices of AlexNet for classification task, which is testing the network on sensor whose measurements are not used for training and mounted at different distances to AE source. First, the network is trained on the measurements obtained from the sensor mounted at close distance to AE source and tested on measurements of the sensor mounted at long distance to AE source. The results show that the model classified symmetrical modes with 100% accuracy, whereas the asymmetrical modes are classified with 74% accuracy as illustrated in Figure 5.5. In contrast, when the network trained on measurements of sensor mounted at long distance to AE source and tested on the measurements of sensor mounted at close distance to AE source classified asymmetrical modes with better accuracy, which is 100%, while the symmetrical modes are classified with 82% accuracy.

Proposed Network

($n_{Training}$=300, $n_{validation}$=100, $n_{testing}$=100)

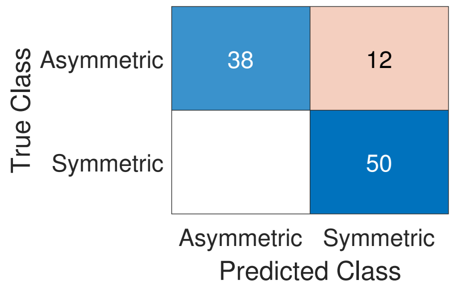

Figure 5.7 Confusion matrix of the proposed network: Trained on S_2 and tested on S_3 measurements

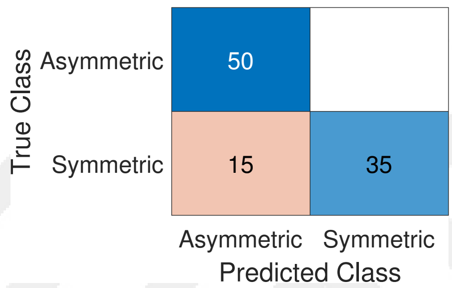

Figure 5.8 Confusion matrix of the proposed network: Trained on S_3 and tested on S_2 measurements

The proposed network, which is trained on measurements obtained from the sensor mounted at close distance to AE source classified symmetric modes with 100% accuracy, whereas the asymmetric modes are classified with 76% accuracy by the same network as it is illustrated in Figure 5.7. On the other hand, the network, which is trained on the measurements of sensor mounted at long distance to AE source classified asymmetrical modes with 100% accuracy, while the symmetric modes are classified with 70% accuracy by the same network as illustrated in Figure 5.8.

The results show that, the regardless of the model architectures, the CNN models classified symmetrical modes with higher accuracy when the models are tested on measurements which undergo more propagation effects compared to measurements used in training. On the other hand, the networks classified asymmetrical modes with higher accuracy, when they are tested on the measurements which undergo less propagation effects compared to measurements used in training process.

5.2 Classification into 4 Label: Symmetric High, Symmetric Low, Asymmetric High and Asymmetric Low

5.2.1 Regular Testing: Training and Testing on Same Sensor Data

AlexNet

($n_{Training}$=300, $n_{validation}$=100, $n_{testing}$=200)

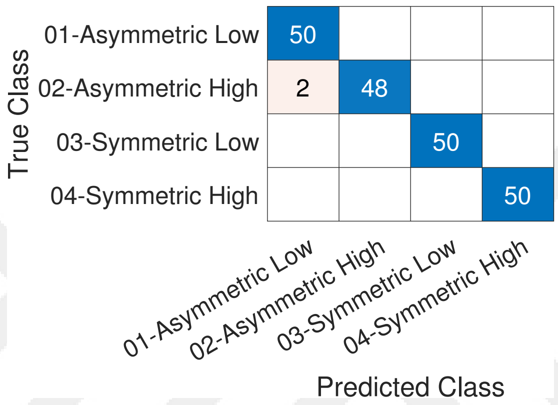

Figure 5.9 Confusion matrix of AlexNet: Trained and tested on S_2 measurements

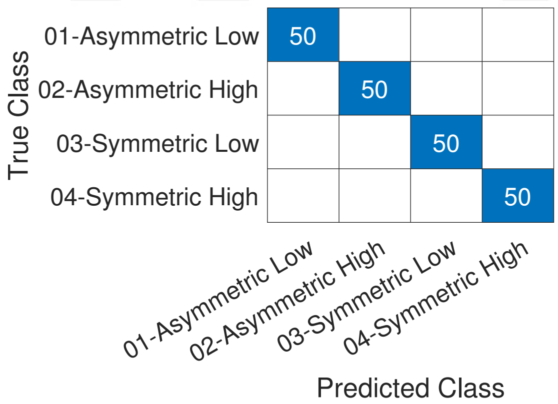

Figure 5.10 Confusion matrix of AlexNet: Trained and tested on S_3 measurements

Fig.5.9 and Fig.5.10 show the confusion matrices of AlexNet on regular testing for both S_2 and S_3 measurements. Overall classification accuracy of AlexNet is 99% for S_2 measurements, whereas S_3 measurements are classified with 100% accuracy.

Proposed Network

($n_{Training}$=300, $n_{validation}$=100, $n_{testing}$=200)

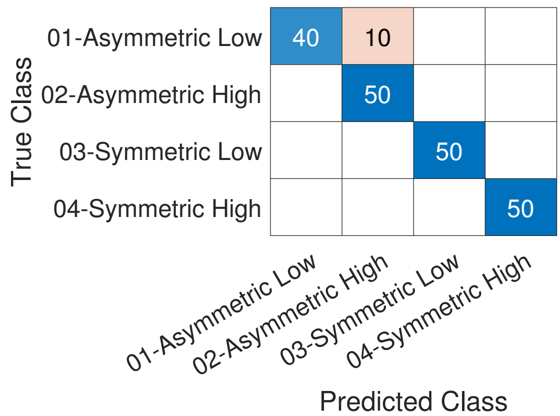

Figure 5.11 Confusion matrix of the proposed network: Trained and tested on S_2 measurements

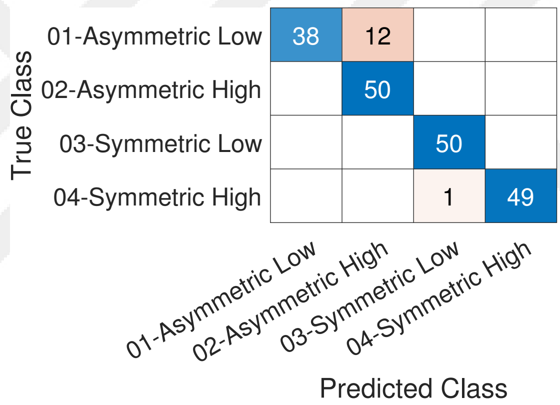

Figure 5.12 Confusion matrix of the proposed network: Trained and tested on S_3 measurements

Confusion matrices of the proposed network on S_2 and S_3 measurements are illustrated in 5.11 and Fig.5.12 respectively. Overall classification accuracy of the model is 95% for S_2 measurements, whereas S_3 measurements are classified with 93.5% accuracy by proposed network.

5.2.2 *Cross-Testing: Training and Testing on Different Sensor Data*

AlexNet

($n_{Training}$=300, $n_{validation}$=100, $n_{testing}$=200)

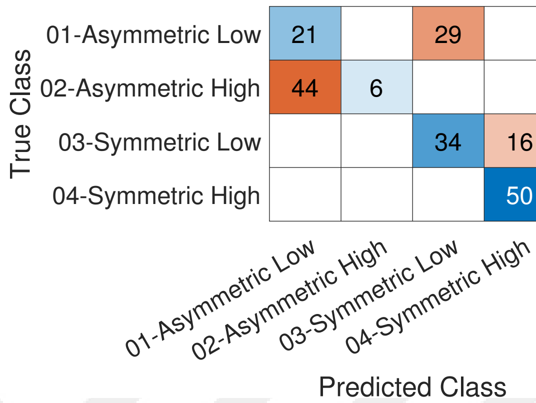

Figure 5.13 Confusion matrix of AlexNet: Trained on S_2 and tested on S_3 measurements

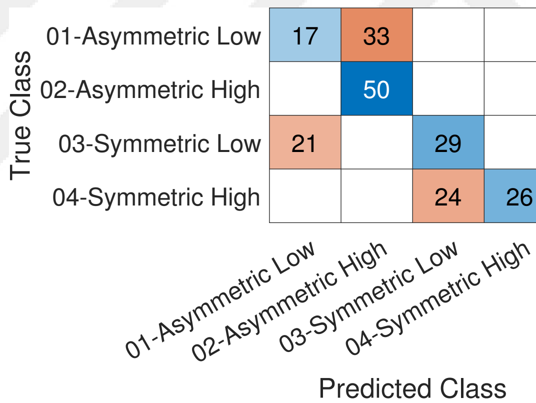

Figure 5.14 Confusion matrix of AlexNet: Trained on S_3 and tested on S_2 measurements

The confusion matrix of AlexNet, which is trained on S_2 and tested on S_3 measurements is illustrated in Fig.5.13. The model classified high amplitude symmetrical modes with 100% accuracy, while high amplitude asymmetrical modes are classified with only 12% accuracy. Furthermore the network classified low amplitude symmetrical modes with higher accuracy compared to low amplitude asymmetrical modes. In contrast, the network, which is trained on S_3 and tested on S_2 measurements classified high amplitude asymmetrical modes with 100% accuracy, whereas high amplitude symmetrical modes are classified with 52% accuracy by the same model as shown in Figure 5.14.

Proposed Network

($n_{Training}$=300, $n_{validation}$=100, $n_{testing}$=200)

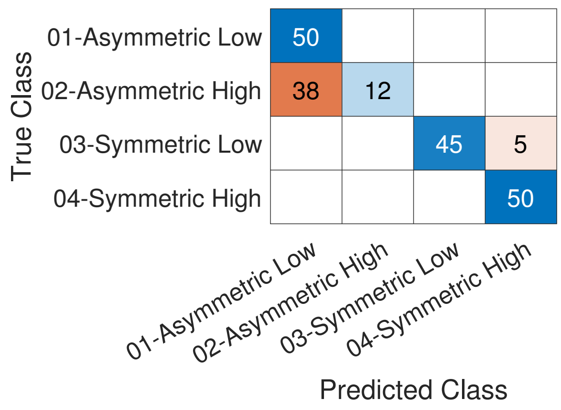

Figure 5.15 Confusion matrix of the proposed network: Trained on S_2 and tested on S_3 measurements

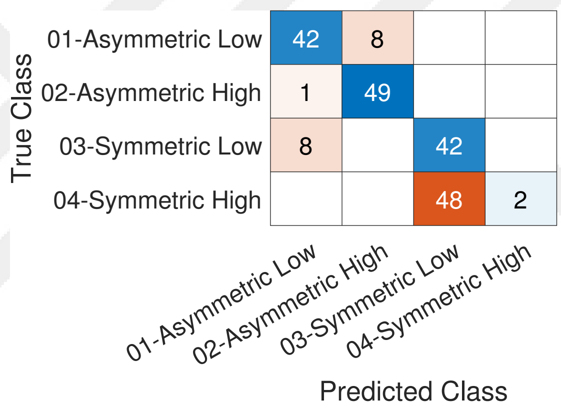

Figure 5.16 Confusion matrix of the proposed network: Trained on S_3 and tested on S_2 measurements

Training and testing procedures, which are applied to AlexNet are also applied to proposed network. Confusion matrices of the proposed network for those procedures are illustrated in Fig.5.15 and Fig.5.16. The model classified particularly high amplitude symmetrical modes with higher accuracy when it is trained and tested on S_2 and S_3 measurements, respectively. In contrast, when the model is trained on S_3 and tested on S_2 measurements, high amplitude asymmetrical modes are classified with high accuracy.

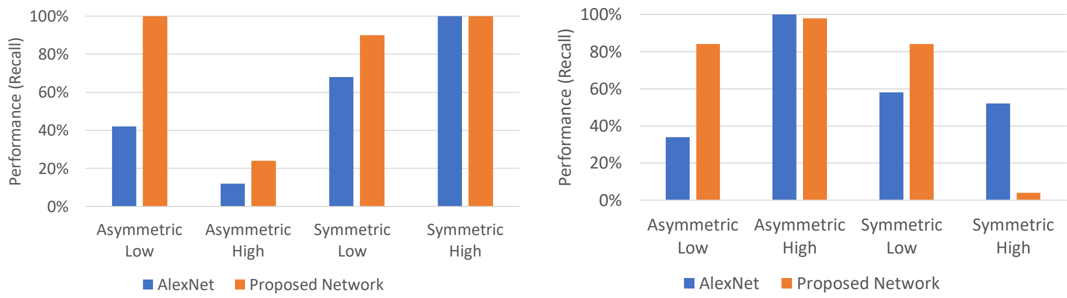

(a) The models trained on S_2 and tested on S_3

(b) The models trained on S_3 and tested on S_2

Figure 5.17 Comparement of AlexNet and proposed network

The overview of the classification results for both network is presented in Figure 5.17. The results show that both network, AlexNet and proposed network, classifies high amplitude symmetrical modes with higher accuracy, when they are trained on S_2 and tested on S_3 measurements as illustrated in Figure 5.17a. In contrast, both CNN network classified high amplitude asymmetrical modes with better accuracy when the models are trained on S_3 measurements and tested on S_2 measurements. In terms of propagation effects on waveform, S_2 measurements represent the waveform undergoing less propagation effects compared to S_3. Therefore it can be concluded that the CNN model more likely classifies symmetrical modes with higher accuracy, if the model is trained on the waveform, which undergoes less propagation effects compared to waveforms used in testing the model. In contrast, the CNN model classifies asymmetrical modes with higher accuracy, if the model is trained on the waveform, which undergoes more propagation effects compared to waveforms used in testing the model.

5.3 Transfer Learning: Fine-tuning Trained Networks on Different Sensor Measurements

In Chapter 5.1 and Chapter 5.2, the CNN models which have different architectures, pre-trained AlexNet and proposed model, are tested on different sensor measurements to observe dependence of classification performance on propagation effects. The applied method also measures that how much are the models capable of generalizing the learned features to use in another domain data such as another sensor, which is mounted at different position according to AE source. The results suggest that the classification accuracy is quite low when the models are tested on another sensor data, although particular dominant wave modes (S_0) or (A_0) are classified with high accuracy dependant on particular sensor data used in training and testing process. In context of SHM, obtaining labelled damage-specific data for different sensors might not be possible or feasible in order to train particular models (Gardner et al., 2020). To be able to address this issue, the present study used transfer learning, which is using the knowledge in a form of weights and biases of trained classifier in one domain to train new network in another domain. In this study, domains are represented by data of different sensors (S_2 and S_3) mounted at different positions according to AE source. The models are fine-tuned with different amount of target domain data to establish a new network for target domain.

This section is divided into two part to show classification performance of different fine-tuned models, fine-tuned AlexNet and fine-tuned proposed network. The classification performance of fine-tuned networks on particular wave modes and overall is presented for 4 label classification scenario. The models are fine-tuned with 20, 40 and 60 training samples. The training process is terminated when the classification accuracy had not been increased five times during the training. Furthermore, five fold cross-validation is used to examine the effect of variance of data on classification performance. The performance of models for each sub-fold is averaged.

5.3.1 *Fine-tuning AlexNet*

In this section, AlexNet is fine-tuned on different number of samples from the data obtained from another sensor, which is mounted at different position according to AE source. The classification performance of the fine-tuned model is presented with the performance of the same model before the model is fine-tuned.

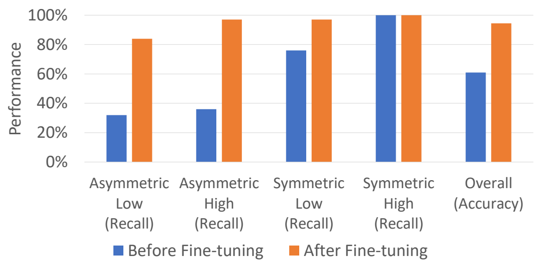

(a) Trained on S_2,
fine-tuned and tested on S_3

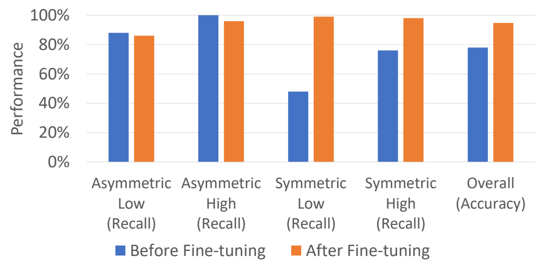

(b) Trained on S_3,
fine-tuned and tested on S_2

Figure 5.18 Effect of fine-tuning on classification performance: Fine-tuning AlexNet on 20 samples to transfer learning

Figure 5.18 illustrates the classification performance of AlexNet after the model is fine-tuned on 20 samples from the data obtained from the another sensor measurements. The fine-tuned models are tested on target domain measurements. The performance of the model on classifying target domain measurements increased in overall as illustrated in Fig.5.18a and Fig.5.18b.

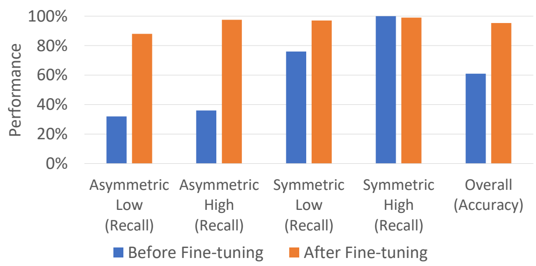

(a) Trained on S_2,
fine-tuned and tested on S_3

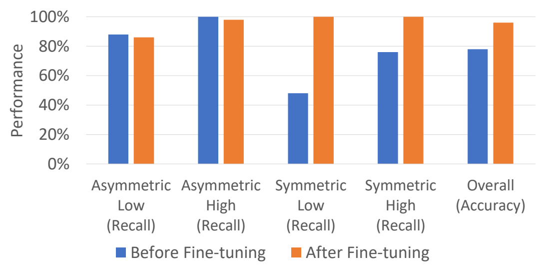

(b) Trained on S_3,
fine-tuned and tested on S_2

Figure 5.19 Effect of fine-tuning on classification performance: Fine-tuning AlexNet on 40 samples to transfer learning

Figure 5.19 illustrates the classification performance of AlexNet after the model is fine-tuned on 40 samples from the data obtained from the another sensor measurements. The fine-tuned models are tested on target domain measurements. The performance of the model on classifying target domain measurements increased in overall as illustrated in Fig.5.19a and Fig.5.19b.

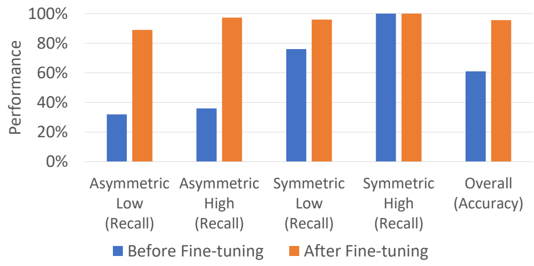

(a) Trained on S_2,
fine-tuned and tested on S_3

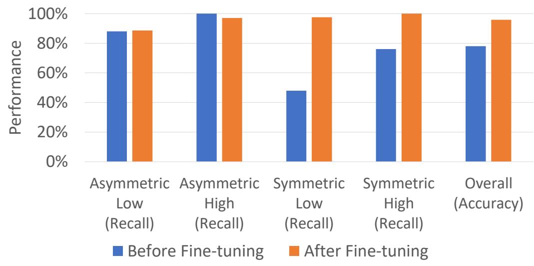

(b) Trained on S_3,
fine-tuned and tested on S_2

Figure 5.20 Effect of fine-tuning on classification performance: Fine-tuning AlexNet on 60 samples to transfer learning

Figure 5.20 illustrates the classification performance of AlexNet after the model is fine-tuned on 60 samples from the data obtained from the another sensor measurements. The fine-tuned models are tested on target domain measurements. The performance of the model on classifying target domain measurements increased in overall as illustrated in Fig.5.20a and Fig.5.20b.

The results showed that the learned features of AlexNet can be transfered into target domain using 20 samples from the target domain to train classifier in context of transfer learning in different sensor measurement. The effect of using more samples has not led to considerable increase in classification performance.

5.3.2 Fine-tuning Proposed Network

In this section, proposed network is fine-tuned on different number of samples obtained from another sensor mounted at different position according to AE source. The classification performance of fine-tuned model is presented with the performance of the same model before the model is fine-tuned.

Figure 5.21 illustrates the classification performance of proposed network after the

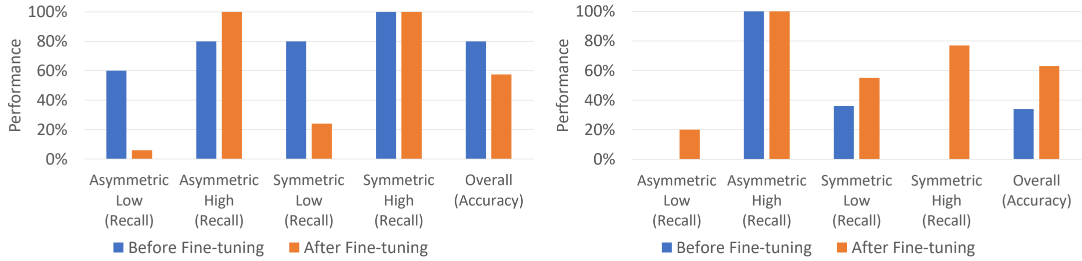

(a) Trained on S_2, fine-tuned and tested on S_3

(b) Trained on S_3, fine-tuned and tested on S_2

Figure 5.21 Effect of fine-tuning on classification performance: Fine-tuning proposed network on 20 samples to transfer learning

model is fine-tuned on 20 samples from the data obtained from the another sensor measurements. The fine-tuned models are tested on target domain measurements. Overall accuracy of the model decreased after the model is fine-tuned on S_3 measurements as shown in Figure 5.21a. In contrast, overall accuracy of the model increased when the model is fine-tuned on S_2 measurements as illustrated in Figure 5.21b.

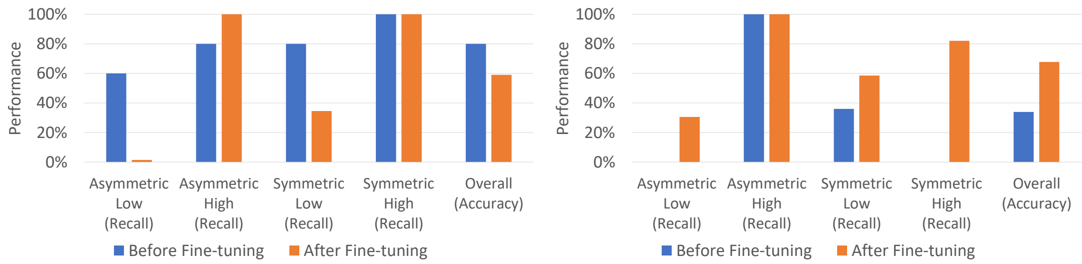

(a) Trained on S_2, fine-tuned and tested on S_3

(b) Trained on S_3, fine-tuned and tested on S_2

Figure 5.22 Effect of fine-tuning on classification performance: Fine-tuning proposed network on 40 samples to transfer learning

Classification performance of the proposed network after the model is fine-tuned on 40 samples from the data obtained from another sensor is illustrated in Figure 5.22. Overall accuracy decreased after the model is fine-tuned on S_3 measurements as shown in Fig. 5.22a, whereas the opposite trend is observed in Fig. 5.22b. Overall accuracy slightly changes in Fig.5.22a and Fig.5.22b compared to models fine-tuned on 20 samples as illustrated in Fig.5.21a and Fig.5.21b.

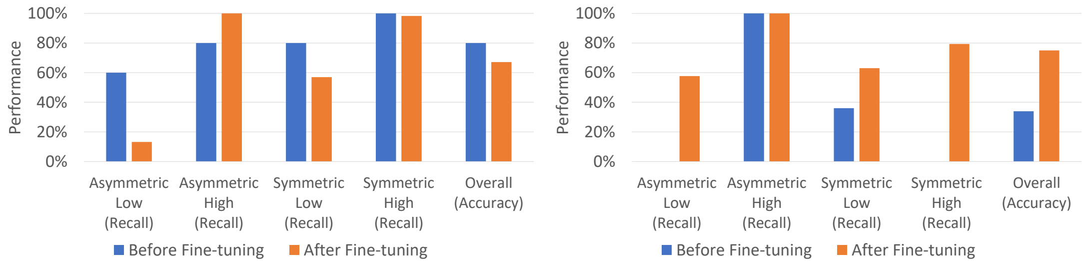

(a) Trained on S_2,
fine-tuned and tested on S_3

(b) Trained on S_3,
fine-tuned and tested on S_2

Figure 5.23 Effect of fine-tuning on classification performance: Fine-tuning proposed network on 60 samples to transfer learning

Figure 5.23 illustrates the classification performance of the proposed network after the model is fine-tuned on 60 samples from the data obtained from the another sensor. The fine-tuned models are tested on target domain measurements. Overall accuracy of the model decreased after the model is fine-tuned on S_3 measurements as shown in Figure 5.23a. In contrast, overall accuracy of the model increased when the model is fine-tuned on S_2 measurements as illustrated in Figure 5.23b.

In conclusion, fine-tuning process led to different classification accuracy on two different architectures, AlexNet and proposed network. However, both of the network classified particular modes such as high amplitude symmetrical and high amplitude asymmetrical modes with better performance after the models are fine-tuned. Furthermore, using more samples for fine-tuning led to slight increase in overall accuracy.

CHAPTER SIX
CONCLUSION

In this study, classification of AE measurements for characterization of damage modes in composites is investigated using convolutional neural networks. In particular, dependence of classification performance on different propagation distances is examined experimentally. Furthermore, transfer learning concept is proposed to train new classifiers for cases in which only limited labelled data is available.

Different damage modes are represented by dominant fundamental Lamb wave modes, S_0 and A_0. These waveforms are generated using PWASs in particular configuration and synchronization and in different amplitudes in order to satisfy variety of damage. Generated waveforms are measured by sensors mounted at different distances to the AE source to address impact of wave propagation on classification performance.

The measured waveforms are converted into time-frequency domain using continuous wavelet transform in order to enhance multimodal and dispersive characteristic of waveforms. The absolute value of wavelet coefficients are normalized to create input images for CNN models.

Two different CNN models, AlexNet and proposed network, which have different architectures are used to classify AE measurements in two different classification tasks. Firstly, CNN models are tested on the sensor measurements on which they are trained. The results showed that both of the networks are capable of classifying measurements with more than 90% accuracy for all classification tasks. Secondly, cross-testing between the sensor measurements is used. The results showed that classification accuracies of the CNN models are decreased significantly. However, despite the decrease in overall accuracies, particular wave modes (S_0 or A_0) are classified with high performance according to propagation distance between AE source and the point at which the waveform is measured. The CNN models, which are trained on data obtained from the sensor mounted at close distance to AE source classified symmetrical modes (S_0) with higher accuracy when they are tested on data obtained from the sensor mounted at long distance to AE source. In contrast, the CNN models which are trained on the measurements obtained from the sensor mounted at long distance to AE source classified asymmetrical modes (A_0) with higher accuracy when they are tested on the measurements obtained from the sensor mounted at close distance to AE source. Based on these results, it can be concluded that the CNN model more likely classifies symmetrical modes (S_0) with higher accuracy if the model is trained on the waveforms which undergo less propagation effects compared to the waveforms used for testing the model. On the other hand, the CNN model more likely classifies asymmetrical modes (A_0) with higher accuracy, if the model is trained on the waveforms which undergo more propagation effects compared to the waveforms used for testing the model.

In context of SHM, obtaining damage-labelled data for the sensors, by which the structure is monitored might not be possible every time. Also, the classifier which is trained on particular sensor measurement is not capable of classifying the measurements of other sensors mounted at different positions in an accurate way due to propagation effects as shown in this study. In order to address this issue, the present study used transfer learning. The CNN models which are trained on particular sensor measurements are fine-tuned on samples from the another sensor. In order to address effect of number of samples used in fine-tuning on performance of fine-tuned model, different number of samples are used. The networks are tested on target domain before and after fine-tuning. The results showed that fine-tuned AlexNet is capable of classifying target domain measurements with high accuracy, while proposed network overall accuracy decreased in one case. However, classification performance of both of the networks increased on particular modes. Furthermore, overall accuracy of the models slightly increased when the models are fine-tuned on more samples.

Although the present study avoided to use random data splitting to increase the repeatability of the classification results, the stochastic nature of the training process due to random weight initialization makes difficult to obtain high repeatable results. The further studies might control the parameters which contribute this random nature of the training process in order to obtain more repeatable results. Furthermore, local minimums during the gradient descent need to be considered. In order to validate the presented results, pencil lead break tests can be used as an artificial AE source in further studies. Moreover, different architectures and classification schemes can be employed to validate the results. Besides, investigating different performance parameters such as precision or specificity may reveal more about the impact of wave propagation on classification results.

REFERENCES

Abdeljaber, O., Avci, O., Kiranyaz, S., & Gabbouj, M. Inman, D. J. (2017). Real-time vibration-based structural damage detection using one-dimensional convolutional neural networks. *Journal of Sound and Vibration*, *388*, 154–170.

Al-Jumaili, S. K. (2016). *Damage assessment in complex structures using acoustic emission*. PhD thesis, Cardiff University, Cardiff, Wales.

Asamene, K., Hudson, L., & Sundaresan, M. (2015). Influence of attenuation on acoustic emission signals in carbon fiber reinforced polymer panels. *Ultrasonics*, *59*, 86–93.

ASTM (2017). *Standard terminology for nondestructive examinations*. West Conshohocken: ASTM International.

Baccar, D. (2015). *Development, implementation, and validation of an acoustic emission-based structural health monitoring system*. PhD thesis, University of Duisburg-Essen, Duisburg, Germany.

Baccar, D., & Soeffker, D. (2017). Identification and classification of failure modes in laminated composites by using a multivariate statistical analysis of wavelet coefficients. *Mechanical Systems and Signal Processing*, *96*, 77–87.

Barre, S., & Benzeggagh, M. L. (1994). On the use of acoustic emission to investigate damage mechanisms in glass-fibre-reinforced polypropylene. *Composites Science and Technology*, *52*(3), 369–376.

Berthelot, J. M., & Rhazi, J. (1990). Acoustic emission in carbon fibre composites. *Composites Science and Technology*, *37*(4), 411–428.

Boeing (2006). Boeing 787: from the ground up. *Boeing Aero*, *24*(04), 17–25.

Charniak, E. (2019). *Introduction to deep learning*. Cambridge: The MIT Press.

Chen, C. (2007). *Ultrasonic and advanced methods for nondestructive testing and material characterization*. Singapore: World Scientific.

Cohen, L. (1995). *Time-frequency analysis*, vol. 778. New Jersey: Prentice hall.

Crivelli, D., Guagliano, M., & Monici, A. (2014). Development of an artificial neural network processing technique for the analysis of damage evolution in pultruded composites with acoustic emission. *Composites Part B: Engineering*, *56*, 948–959.

De Groot, P. J., Wijnen, P. A. M., & Janssen, R. B. F. (1995). Real-time frequency determination of acoustic emission for different fracture mechanisms in carbon/epoxy composites. *Composites Science and Technology*, *55*(4), 405–412.

Eaton, M. (2007). *Acoustic Emission (AE) monitoring of buckling and failure in carbon fibre composite structures*. PhD thesis, Cardiff University, Cardiff, Wales.

Eaton, M., May, M., Featherston, C., Holford, K., Hallet, S., & Pullin, R. (2011). Characterisation of damage in composite structures using acoustic emission. *Journal of Physics: Conference Series*, *305*(1), 012086.

Ebrahimkhanlou, A., & Salamone, S. (2018). Single-sensor acoustic emission source localization in plate-like structures using deep learning. *Aerospace*, *5*(2), 50.

Farrar, C. R., & Worden, K. (2007). An introduction to structural health monitoring. *Philosophical Transactions of the Royal Society A: Mathematical, Physical and Engineering Sciences*, *365*(1851), 303–315.

Fukushima, K., & Miyake, S. (1982). Neocognitron: A self-organizing neural network model for a mechanism of visual pattern recognition. In *Competition and Cooperation in Neural Nets*, *45*, 267–285.

Gao, R. X., & Yan, R. (2010). *Wavelets: Theory and applications for manufacturing*. New York: Springer Science & Business Media.

Gardner, P., Liu, X., & Worden, K. (2020). On the application of domain adaptation in structural health monitoring. *Mechanical Systems and Signal Processing*, *138*, 106550.

Giurgiutiu, V. (2007). *Structural health monitoring: with piezoelectric wafer active sensors*. Burlington: Elsevier.

Giurgiutiu, V. (2015). *Structural health monitoring of aerospace composites*. Cambridge: Academic Press.

Glorot, X., Bordes, A., & Bengio, Y. (2011). Deep sparse rectifier neural networks. In *Proceedings of the Fourteenth International Conference on Artificial Intelligence and Statistics*, *15*, 315–323.

Godin, N., Huguet, S., Gaertner, R., & Salmon, L. (2004). Clustering of acoustic emission signals collected during tensile tests on unidirectional glass/polyester composite using supervised and unsupervised classifiers. *Ndt & E International*, *37*(4), 253–264.

Godin, N., Reynaud, P., & Fantozzi, G. (2018). *Acoustic Emission and Durability of Composite Materials*. New York: Wiley Online Library.

Gorman, M. R. (1991). Plate wave acoustic emission. *The Journal of the Acoustical Society of America*, *90*(1), 358–364.

Grosse, C., & Ohtsu, M. (2008). *Acoustic emission testing*. Leipzig: Springer.

Gu, J., Wang, Z., Kuen, J., Ma, L., Shahroudy, A., Shuai, B., Liu, T., Wang, X., Wang, G., Cai, J., & Tsuhan, C. (2018). Recent advances in convolutional neural networks. *Pattern Recognition*, *77*, 354–377.

Gutkin, R., Green, C. J., Vangrattanachai, S., Pinho, S. T., Robinson, P., & Curtis, P. T. (2011). On acoustic emission for failure investigation in cfrp: Pattern recognition and peak frequency analyses. *Mechanical Systems and Signal Processing*, *25*(4), 1393–1407.

Hamstad, M. A. (2007). Acoustic emission signals generated by monopole (pencil lead break) versus dipole sources: finite element modeling and experiments. *Journal of Acoustic Emission*, *25*, 92–106.

Haykin, S. (1994). *Neural networks: a comprehensive foundation*. New Jersey: Prentice Hall.

Hellier, C. J. (2003). *Handbook of Non-Destructive Evaluation*. New York: McGraw-Hill.

Ioffe, S., & Szegedy, C. (2015). Batch normalization: Accelerating deep network training by reducing internal covariate shift. *arXiv preprint arXiv:1502.03167*, 448–456.

Kelleher, J. D. (2019). *Deep learning*. Cambridge: MIT press.

Kharrat, M., Placet, V., Ramasso, E., & Boubakar, M. L. (2018). Influence of damage accumulation under fatigue loading on the ae-based health assessment of composite materials: Wave distortion and ae-features evolution as a function of damage level. *Composites Part A: Applied Science and Manufacturing*, *109*, 615–627.

Kishi, T., Ohtsu, M., & Yuyama, S. (2000). *Acoustic emission-beyond the millennium*. Oxford: Elsevier.

Krizhevsky, A., Sutskever, I., & Hinton, G. E. (2012). Imagenet classification with deep convolutional neural networks. *Advances in Neural Information Processing Systems*, *25*, 1097–1105.

LeCun, Y., Bengio, Y., & Hinton, G. (2015). Deep learning. *nature*, *521*(7553), 436–444.

LeCun, Y., Boser, B. E., Denker, J. S., Henderson, D., Howard, R. E., Hubbard, W. E., & Jackel, L. D. (1990). Handwritten digit recognition with a back-propagation network. In *Advances in Neural Information Processing Systems*, 396–404.

Leis, J. (2011). *Digital signal processing using MATLAB for students and researchers*. New York: Wiley Online Library.

Maillet, E., Baker, C., Morscher, G. N., Pujar, V. V., & Lemanski, J. R. (2015). Feasibility and limitations of damage identification in composite materials using acoustic emission. *Composites Part A: Applied Science and Manufacturing*, *75*, 77–83.

Mazumdar, S. (2001). *Composites manufacturing: materials, product, and process engineering*. Florida: CrC press.

Newland, D. E. (2012). *An introduction to random vibrations, spectral & wavelet analysis*. New York: Dover Publications.

Ni, Q. Q., & Iwamoto, M. (2002). Wavelet transform of acoustic emission signals in failure of model composites. *Engineering Fracture Mechanics*, *69*(6), 717–728.

Nielsen, M. A. (2015). *Neural networks and deep learning*. San Francisco: Determination Press.

Ozevin, D., Greve, D. W., Oppenheim, I. J., & Pessiki, S. P. (2006). Resonant capacitive mems acoustic emission transducers. *Smart Materials and Structures*, *15*(6), 1863.

PI Ceramic GmbH (n.d.). Retrieved February 4, 2020, from https://www.piceramic.com/en/products/piezoelectric-materials/.

Pollock, A. A. (1986). Classical wave theory in practical ae testing. *Progress in Acoustic Emission III-JAP Society of Non-Destructive Testing*, 708–721.

Prosser, W. H. (1996). Advanced ae techniques in composite materials research. *Journal of Acoustic Emission*, *14*(3-4), 1–11.

Ramirez-Jimenez, C., Papadakis, N., Reynolds, N., Gan, T. H., Purnell, P., & Pharaoh, M. (2004). Identification of failure modes in glass/polypropylene composites by means of the primary frequency content of the acoustic emission event. *Composites Science and Technology*, *64*(12), 1819–1827.

Rose, J. L. (2014). *Ultrasonic guided waves in solid media*. Cambridge: Cambridge University Press.

Russel D. (2016). *Rayleigh surface waves*. Retrieved December 31, 2019, from https://www.acs.psu.edu/drussell/Demos/waves/wavemotion.html.

Sause, M. G. R. (2011). Investigation of pencil-lead breaks as acoustic emission sources. *Journal of Acoustic Emission*, *29*, 184–196.

Scruby, C. B. (1987). An introduction to acoustic emission. *Journal of Physics E: Scientific Instruments*, *20*(8), 946.

Srivastava, N., Hinton, G., Krizhevsky, A., Sutskever, I., & Salakhutdinov, R. (2014). Dropout: a simple way to prevent neural networks from overfitting. *The Journal of Machine Learning Research*, *15*(1), 1929–1958.

Stanford (2019). Retrieved January 27, 2020, from https://www.acs.psu.edu/drussell/Demos/waves/wavemotion.html.

Su, Z., & Ye, L. (2009). *Identification of damage using Lamb waves: from fundamentals to applications,* (*48*). Berlin: Springer Science & Business Media.

Su, Z., Ye, L., & Lu, Y. (2006). Guided lamb waves for identification of damage in composite structures: A review. *Journal of Sound and Vibration*, *295*(3-5), 753–780.

Tabian, I., Fu, H., & Khodaei, S. Z. (2019). A convolutional neural network for impact detection and characterization of complex composite structures. *Sensors*, *19*(22), 4933.

Taspinar, R. (2018). Retrieved January 20, 2020, from https://ataspinar.com/2018/12/21/a-guide-for-using-the-wavelet-transform-in-machine-learning/.

Valentin, D., Bonniau, P. H., & Bunsell, A. R. (1983). Failure mechanism discrimination in carbon fibre-reinforced epoxy composites. *Composites*, *14*(4), 345–351.

Wang, X., Lu, Y., & Tang, J. (2008). Damage detection using piezoelectric transducers and the lamb wave approach: I. system analysis. *Smart Materials and Structures*, *17*(2), 025033.

Wirtz, S. (2015). *Qualication of AE measurements for damage classication in composites*. Master's thesis, University of Duisburg-Essen, Duisburg, Germany.

Wirtz, S. F., Bach, S., & Soeffker, D. (2019). Experimental results of acoustic emission attenuation due to wave propagation in composites. In *Proceedings of the Annual Conference of the PHM Society*, *11*, 1–7.

Yosinski, J., Clune, J., Bengio, Y., & Lipson, H. (2014). How transferable are features in deep neural networks? In *Advances in Neural Information Processing Systems*, 3320–3328.

APPENDICES

Appendix 1 - Matlab code for creating CWT images

```
clc;clear;
% Importing measurements
datas=matfile('01 A -100 %_Hits'); whos(datas)
hits=datas.hits;
[nSensor,nSignal,nSample]=size(hits);

fs=4e6; % sampling frequency
fb = cwtfilterbank('SignalLength',nSample...
,'VoicesPerOctave',12,'SamplingFrequency',fs) % filtering

% Wavelet transform of measurements
for i=1:nSignal
signal{i}=squeeze(hits(2,i,1:end));
cfs = abs(wt(fb,signal{i}));

% Converting wavelet coefficients into RGB images
im = ind2rgb(im2uint8(rescale(cfs)),jet(128));
imgLoc = imageRoot;
imFileName = strcat('P2_B',num2str(i),'.jpg');%%
imwrite(imresize(im,[227 227]),fullfile(imgLoc,imFileName));

end
```

Appendix 2 - Matlab code for pre-trained AlexNet

```
clc;clear;
% Defining imagedatastores for data
dirImdsTrain=fullfile('file_path_for_training_data');
imdsTrain=imageDatastore(dirImdsTrain,'IncludeSubFolders'...
    ,true, 'LabelSource','foldernames');
dirImdsVal=fullfile('file_path_for_validation_data');
imdsVal=imageDatastore(dirImdsVal,'IncludeSubFolders'...
    ,true,'LabelSource','foldernames');
dirImdsTest=fullfile('file_path_for_regularTest_data');
imdsTest=imageDatastore(dirImdsTest,'IncludeSubFolders'...
    ,true,'LabelSource','foldernames');
dirImdsTest2=fullfile('file_path_for_crossTest_data');
imdsTest2=imageDatastore(dirImdsTest2,'IncludeSubFolders'...
    ,true,'LabelSource','foldernames');

% Calling pre-trained alexNet
net = alexnet

% Transfer pre-trained layers except the for last 3 layers
layersTransfer = net.Layers(1:end-3);
% Define number of classification label using data
numClasses = numel(categories(imdsTrain.Labels))
% Define the new layers
layers = [
layersTransfer
fullyConnectedLayer(numClasses,'WeightLearnRateFactor',...
    20,'BiasLearnRateFactor',20)
softmaxLayer
classificationLayer];
```

```
% Setting training options
options = trainingOptions('sgdm', ...
'MiniBatchSize',10,...
'InitialLearnRate',1e-4, ... %
'ValidationData',imdsVal,...
'ValidationFrequency',20,...
'Shuffle','every-epoch', ...
'ExecutionEnvironment','cpu',...
'Plots','none',...
'OutputFcn',@(info)stopIfAccuracyNotImproving(info,20));

% Fine-tuning pre-trained network with new data
netTransfer = trainNetwork(imdsTrain,layers,options);
clear net

% Classification-Regular Testing
[YPred,probs] = classify(netTransfer,imdsTest...
    ,'ExecutionEnvironment','cpu');
figure()
cm=confusionchart(imdsTest.Labels,YPred...
    ,'InnerPosition',[0.5 0.5 0.5 0.5])
cm.FontSize=18
% Classification-Cross Testing
[YPred2,probs] = classify(netTransfer,imdsTest2...
    ,'ExecutionEnvironment','cpu');
figure()
cm=confusionchart(imdsTest2.Labels,YPred2...
    ,'InnerPosition',[0.5 0.5 0.5 0.5])
cm.FontSize=18
```

```matlab
%------------------------------------------------
% The function remains training if the accuracy is not
% improving N times during the validation
% The source: MatLAB documentation
function stop = stopIfAccuracyNotImproving(info,N)
stop = false;

persistent bestValAccuracy
persistent valLag

if info.State == "start"
    bestValAccuracy = 0;
    valLag = 0;

elseif ~isempty(info.ValidationLoss)

    if info.ValidationAccuracy > bestValAccuracy
        valLag = 0;
        bestValAccuracy = info.ValidationAccuracy;
    else
        valLag = valLag + 1;
    end

    if valLag >= N
        stop = true;
    end

end

end
```

Appendix 3 - Matlab code for Proposed Network

```
clc;clear;
% Defining imagedatastores for data
dirImdsTrain=fullfile('file_path_for_training_data');
imdsTrain=imageDatastore(dirImdsTrain,'IncludeSubFolders'...
    ,true, 'LabelSource','foldernames');
dirImdsVal=fullfile('file_path_for_validation_data');
imdsVal=imageDatastore(dirImdsVal,'IncludeSubFolders'...
    ,true,'LabelSource','foldernames');
dirImdsTest=fullfile('file_path_for_regularTest_data');
imdsTest=imageDatastore(dirImdsTest,'IncludeSubFolders'...
    ,true,'LabelSource','foldernames');
dirImdsTest2=fullfile('file_path_for_crossTest_data');
imdsTest2=imageDatastore(dirImdsTest2,'IncludeSubFolders'...
    ,true,'LabelSource','foldernames');

% Defining Network Architecture
numClasses = numel(categories(imdsTrain.Labels))
layers = [
imageInputLayer([227 227 3])
convolution2dLayer(3,8,'Padding','same')
batchNormalizationLayer
reluLayer
maxPooling2dLayer(2,'Stride',2)
dropoutLayer(0.5)
convolution2dLayer(3,16,'Padding','same')
batchNormalizationLayer
reluLayer
maxPooling2dLayer(2,'Stride',2)
dropoutLayer(0.5)
```

```
convolution2dLayer(3,32,'Padding','same')
batchNormalizationLayer
reluLayer
dropoutLayer(0.5)
fullyConnectedLayer(numClasses)
softmaxLayer
classificationLayer];

% Setting training options
options = trainingOptions('sgdm', ...
'MiniBatchSize',10,...
'InitialLearnRate',1e-4, ... %
'ValidationData',imdsVal,...
'ValidationFrequency',20,...
'Shuffle','every-epoch', ...
'ExecutionEnvironment','cpu',...
'Plots','none',...
'OutputFcn',@(info)stopIfAccuracyNotImproving(info,20));

% Training network
netProposed = trainNetwork(imdsTrain,layers,options);
clear layers

% Classification-Regular Testing
[YPred,probs] = classify(netProposed,imdsTest...
    ,'ExecutionEnvironment','cpu');
figure()
cm=confusionchart(imdsTest.Labels,YPred...
    ,'InnerPosition',[0.5 0.5 0.5 0.5])
cm.FontSize=18
```

```
% Classification-Cross Testing
[YPred2,probs] = classify(netProposedr,imdsTest2...
    ,'ExecutionEnvironment','cpu');
figure()
cm=confusionchart(imdsTest2.Labels,YPred2...
    ,'InnerPosition',[0.5 0.5 0.5 0.5])
cm.FontSize=18

%--------------------------------------------------
% The function remains training if the accuracy is not
% improving N times during the validation
% The source: MatLAB documentation
function stop = stopIfAccuracyNotImproving(info,N)
stop = false;

persistent bestValAccuracy
persistent valLag

if info.State == "start"
    bestValAccuracy = 0;
    valLag = 0;

elseif ~isempty(info.ValidationLoss)

    if info.ValidationAccuracy > bestValAccuracy
        valLag = 0;
        bestValAccuracy = info.ValidationAccuracy;
    else
        valLag = valLag + 1;
    end
```

```
        if valLag >= N
            stop = true;
        end

    end

    end
```